Geomorphic analysis of active fold growth and landscape evolution in the central Qiulitage fold belt, southern Tian Shan, China

Bernard Delcaillau, Fabien Graveleau, Dimitri Saint Carlier, Gang Rao, Maryline Le Béon, Julien Charreau, Maëlle Nexer

2021-11-25

Geomorphic analysis of active fold growth and landscape evolution in the central Qiulitage fold belt, southern Tian Shan, China

Bernard Delcaillau[1], Fabien Graveleau[2], Dimitri Saint Carlier[3], Gang Rao[4], Maryline Le Béon[5], Julien Charreau[6], Maelle Nexer[7]

[1-] Normandie Univ, UniCaen, UniRouen, CNRS, M2C, 14000 Caen, F14000 Caen France
[2-] Univ. Lille, CNRS, Univ. Littoral Côte d'Opale, UMR 8187, LOG, Laboratoire d'Océanologie et de Géosciences, F 59000 Lille, France
[3-] Université de Lorraine, Centre de Recherches Pétrographiques et Géochimiques, UMR 7358 CNRS-UL, 15 rue Notre Dame des Pauvres, B.P. 20, 54501 Vandoeuvre lès Nancy, France
[4-] School of Geoscience and Technology, Southwest Petroleum University, Chengdu 610500, China
[5-] National Central University, Graduate Institute of Applied Geology, Taoyuan City, 32001 Taiwan
[6-] Ecole Nationale Supérieure de Géologie de Nancy Centre de Recherches Pétrographiques et Géochimiques 15, rue Notre Dame des Pauvres 54500 Vandoeuvre les Nancy, France
[7-] France-Energies marines, Brest, France
Contact : bernard.delcaillau@unicaen.fr

Abstract

The Qiulitage fold-and-thrust system in the Kuqa foreland is a prominent NE-SW trending relief associated with active thrust-related folding in the southern Tian Shan. Based on open-access DEMs and field work, we carried out a detailed geomorphologic analysis of the Qiulitage topography based on drainage network characteristics and several morphometric indices. Our results suggest that the Qiulitage fold belt is composed of six morphological units, which are statistically confirmed by a principal component analysis. These morphologic structures have interacted during both vertical growth and lateral

propagation of the folds, associated with different patterns of fold connection and deformation partitioning. The structural evolution of the Qiulitage fold belt has significantly influenced major rivers crossing the fold belt and minor ones developing on the fold ridges. We finally propose a morphotectonic evolution of the fold belt integrating the influence of *décollement* distribution, deep inherited structures, and changes in shortening amount.

Keywords: Qiulitage fold belt, fault-related fold, geomorphological analysis, morphometric indices, Tian Shan.

1. Introduction

Geomorphic surfaces, such as alluvial fans, fluvial terraces or drainage basins, are useful markers of active tectonics (*e.g.,* Hardy and Poblet, 1994; Delcaillau et al., 1998; Dolan and Avouac, 2007, Amos et al., 2010, Burbank & Anderson, 2011) that allow documentation of the kinematic evolution of fault-related folds in mountain belts (*e.g.,* Suppe, 1983; Suppe and Medwedeff, 1984). Numerous studies have analyzed the along-strike changes in morphology of active fault-related folds to understand the mechanisms of anticline growth (*e.g.,* Jackson et al., 1996; Mueller and Talling, 1997; Delcaillau et al., 1998; Ramsey et al., 2007; Bull, 2009; Bretis et al., 2011; Keller and DeVecchio, 2013; Collignon et al., 2016; Giampaoli and Rojas Vera, 2018; Sissakian et al., 2019; Bahrami et al., 2020). For instance, relationships between the fold growth and the underlying active thrusts or *décollements* can be decrypted using the associated analyses of structural and geomorphic features, and by dating deformed geomorphic surfaces (*e.g.,* Keller et al., 1998; Jackson et al., 2002; Hetzel et al., 2004; Bennett et al., 2005). In addition, frontal anticlines above active thrust faults typically display drainage

and channel anomalies (*e.g.,* knickpoints) that evidence the landform evolution in response to tectonic and climatic forcings (*e.g.,* Poisson and Avouac, 2004, Boulton et al., 2014, Guerit et al., 2016). As pointed out by Jackson et al. (1998), the shape of landscapes and their drainage networks constitute a response of landforms to tectonic processes (*i.e.,* uplift and subsidence), more or less variably modulated by lithological parameters. The reconstitution of drainage pattern evolution, combined with the growth history of fold belts, contributes to understanding the evolution of mountain belts. In this paper, we address open questions such as 1) how landforms record fold growth (structural relief, topographic emergence, lateral propagation), and 2) how distribution of deformation within a fold belt is recorded at the catchment and topographic ridge scale. We examine the topography of a 200 km long structure, the Qiulitage fold belt, located at the southern margin of the Kuqa fold-and-thrust belt at the piedmont of southern Tian Shan, NW China (Fig. 1A). We investigate the landscape evolution of this active thrust-related fold system in its central part and document: i) the geomorphological response of landforms to differential uplift along the anticlinal ridges, and ii) how lateral propagation of folding is recorded by catchments and drainage networks. We used SRTM and ASTER DEMs (30 m resolution) to investigate the geomorphological properties of the study area, and explore how morphometric indices and topographic profiles record fold growth. We used morphometric indices such as drainage basin area, basin local relief, hypsometric integral, channel steepness index and incision (*e.g.,* Doornkamp and King, 1971; Schumm, 1977; Morisawa and Hack, 1985; Willemin and Knuepfer, 1994; Jackson et al., 1996), which allowed us to classify drainage basins along the folds according to their morphometric

signatures. Our results lead us to propose a geomorphic evolution of Qiulitage drainage basins in relation to the different styles of folding, and probable changes in rates of uplift.

2. Geological setting

2.1. The Tian Shan range

The Tian Shan is an intracontinental mountain range in Central Asia located to the north of the Tibetan Plateau. It is bounded by the Junggar and Tarim foreland basins, to the north and south, respectively (Fig. 1). During the Mesozoic, the Tian Shan is generally thought to be weakly active (Hendrix et al., 1994; Jolivet et al., 2010), whereas it has been strongly reactivated since the Cenozoic due to the collision between the Indian and the Eurasian plates (Molnar and Tapponnier, 1975; Tapponnier and Molnar, 1979). Fold and thrust belts along the northern and southern flanks of the Tian Shan have accommodated the propagation of deformation and the widening of the mountain belt (Avouac et al., 1993; Hendrix et al., 1994; Yin et al., 1998; Burchfiel et al., 1999; Charreau et al., 2005; Sun and Zhang, 2009; Sun et al., 2009; Jolivet et al., 2010; Qiu et al., 2019; Gao et al., 2020). GPS observations indicate that about 20 mm/yr of horizontal shortening is accommodated across the whole Tian Shan range (Abdrakhmatov, 1996; Zubovich et al., 2010). In the southern Tian Shan, GPS data suggest that about 5 mm/yr are presently accommodated across the Kuqa to Korla mountain fronts (Yang et al., 2008).

2.2. Structures of the Qiulitage fold belt

The Kuqa fold-and-thrust belt (KFTB) is located in the southern foothills of the Tian Shan mountains (Fig. 1A). It represents a major structural feature that develops in a Mesozoic and Cenozoic basin along the northern Tarim margin (Métivier and Gaudemer, 1997). Most of the stratigraphic sequence is composed of alternating layers of sandstones, shales and conglomerates, with very few carbonates (Fig. 2). Three peculiar formations are important due to their significant structural role in the deformation of the KFTB: these are the Jurassic coal strata, the Paleocene-Eocene evaporites and the early Miocene evaporitic strata (gypsum and halite). The latter two constitute a weak rheology in which major *décollement* levels controlling fault-related folds and thrusts are rooted (Wang et al., 2011) (Fig. 1C).

The Qiulitage structures have been constrained by a dense dataset of bedding measurements, industrial seismic profiles and wells (Wang et al., 2011; Li et al., 2012; Tang et al., 2017; Izquierdo-Llavall et al., 2018). These data illustrate how the structural style evolves from a foreland-ward vergent dual fold system in the west (sections 1-3 in Fig. 1C) to a single monocline structure controlled by a back-thrust or anticline further east (sections 4 and 5 in Fig. 1C). Seismic profiles and well analyses have demonstrated that evaporites and salt-related tectonics have played an important control on the kinematics of the KFTB (Chen et al., 2004; Xu and Zhou, 2007; Li et al., 2012; Wang et al., 2011; Yu et al., 2014; Zhao and Wang, 2016; Tang et al., 2004; Tang et al., 2015). Early salt flow related to syntectonic deposition might have played an important role on the nucleation of folds (Li et al., 2012; Zhao and Wang, 2016).

In detail, the Northern Qiulitage anticline (NQA) crops out with steeply to shallowly north-dipping beds in the northern limb, and mostly subvertical to overturned beddings in the

southern limb (sections 1-4 Fig. 1C). The southern limb is cut by a steeply-dipping south vergent thrust (*i.e.,* the Northern Qiulitage Thrust - NQT). The Southern Qiulitage anticline (SQA) is a tight fault-related fold characterized by steeply dipping to overturned northern and southern limbs, and a sub-vertical north-verging thrust in the core (*i.e.,* the Southern Qiulitage Thrust, SQT). Between the northern and southern Qiulitage folds, two small intermontane basins are filled with Quaternary deposits (Figs. 1B and 3B). The western intermontane basin (WIB) has a simple syncline shape (section 3 in Fig. 1C), whereas the eastern intermontane basin (EIB) is overthrusted by the NQT. Restoration of seismic sections across the Qiulitage fold belt suggests a similar amount of shortening of ~ 12-14 km (Li et al., 2012; Izquierdo-Llavall et al., 2018; Pla, 2019), although some local higher values (16.5 km; section 4) have been estimated (Fig. 1B). The analysis of dip measurements allows recognition of growth strata and suggests that the NQA has initiated slightly subsequent to the SQA (Izquiedo-Llavall, et al., 2018). The initiation of the KFTB growth could date back to late Miocene (Hubert-Ferrari et al., 2007; Wang et al., 2011; Li et al., 2012, Tian et al., 2016; Tang et al., 2017; Charreau et al., 2020) and two pulses of accelerations in fold growth may have occurred during the Pliocene and the Pleistocene times (*e.g.,* Li et al., 2012; Charreau et al., 2020).

3. Methodology

In order to characterize the structural processes that control the growth and the evolution of the central Qiulitage fold belt, we analyzed landforms at meter to kilometre scales based on field studies and by analyzing Digital Elevation Models (DEM) and satellite images.

DEM data were collected from the NASA SRTM V.4.0 (90 m resolution) and ASTER programs (30 m resolution), whilst satellite images were extracted from Google Earth®. Based on these available datasets, we extracted 250 drainage basins for which we mapped and calculated the following morphometric parameters and geomorphic indices described in more detail hereafter: basin area (A), hypsometry (HI), basin asymmetry factor (A_f), elongation ratio (R_e), local relief (Δ_z), fluvial incision factor (I_f), normalized mean elevation, and normalized steepness index (k_{sn}). Finally, we conducted an ascending hierarchical classification to separate the investigated drainage basins into several classes with similar geomorphological characteristics. Our goal was to observe whether drainage basins that share similar geomorphic characteristics are regionally separated or clustered within a specific zone of the Qiulitage landscape (Table 1). Then, from these classes and their location, our goal was to constraint the morphotectonic evolution of the Qiulitage fold belt and ultimately its growth history.

3.1. Topography

The Qiulitage fold belt between 81.5° and 83°E in longitude is split into two SW-NE parallel topographic ridges (Figs. 1B and 3). The Qiulitage anticline belt is a 225 km long fault-bend fold, 5-7 km in width and presenting up to ~1000 m of relief (Hubert-Ferrari et al., 2007). New morphometric data and the well-preserved geomorphology provide a natural laboratory for exploring the detailed spatio-temporal evolutionary processes of a “mature fold” belt. The present structural relief of the Qiulitage fold-belt shows strong differences in elevation from west to east (Fig. 3): from 1500 to 2083 m for the Northern Qiulitage anticline of and from 1150 to 2174 m for the Southern Qiulitage anticline. The southern ridge is about 165 km long,

and it is composed of the Southern Qiulitage, Kuqatawu and Misikantage anticlines. The northern ridge is much shorter (about 90 km long), consisting of the Northern Qiulitage and Yakelike anticlines. We extracted topographic profiles along the crestline for both ridges (light blue lines, Fig. 3B) so as to analyze how topography evolves along the fold belt. We also measured valley incision (If) along a mid-flank profile (yellow lines) for both the northern and southern ridges to document the amplitude of incision along the fold limbs. Results indicate that both ridges are segmented with several domains of constant or increasing crestline elevation or incision values. This leads us to divide the fold belt into six morphostructures (MS1 to MS6), which are often separated either by water gaps or wind gaps (Fig. 3). Water gaps correspond to valleys that were carved during fold growth and that still host a flowing stream, whereas wind gaps constitute similar valleys that are presently dry and uplifted. Unfortunately, we cannot confirm whether the wind gaps preserve alluvial deposits, nor can we document whether transitions between adjacent morphostructures are controlled by structural features (fold tip, faults, etc.).

3.2. Drainage basin area

The drainage basin area corresponds to the planar area for each item. Sharp changes in area across a fold crestline are often linked to fold growth mechanisms and illustrate particularly mature fault-related folds (*e.g.,* Delcaillau et al., 1998). Additionally, sharp changes in basin area between adjacent catchments can reflect upstream/downstream drainage captures or basin shrinking through interfluve and crestline migration, that are driven by growth mechanisms or erosion asymmetry (Bonnet et al., 2009). Progressive

changes along the fold strike can reflect fold lateral propagation dynamics (Mueller and Talling, 1997; Delcaillau et al., 1998).

3.3. Drainage basin hypsometry

The drainage basin hypsometry accounts for the distribution of elevation in a given area of a landscape (Strahler, 1952; Ohmiri, 1993). It can be plotted as the hypsometric curve and calculated through the Hypsometric Integral (HI). HI is defined as the area below the hypsometric curve and can be calculated with the formula (Pike and Wilson, 1971):

$$HI = \frac{\mathrm{h}_{\mathrm{mean}} - h_{min}}{h_{\mathrm{max}} - \mathrm{h}_{min}} \qquad \text{Equation 1}$$

where h_{mean}, h_{min} and h_{max} are the mean, minimum and maximum elevation, respectively. HI is a measurement of the erosional state or geomorphic age of a drainage basin as it represents the volume of drainage basin remaining above a basal plane of reference. The shape of the hypsometric curve reflects the evolution stage of the drainage basin (Strahler, 1952), and therefore its erosion history. Particularly, it is either young when the hypsometric curve is convex-upward, mature when the curve is concave-upwards, or intermediate when the curve is S-shaped. Hi is independent of basin area, so it provides a valuable tool to compare drainage basins to one another. The hypsometric integral could indicate not only the rate of geomorphological change that take place in watersheds (*e.g.,* Ciccacci et al., 1992), but it can also evidence the morphogenetic response of lateral propagation of an active anticline (*e.g.,* Delcaillau et al., 1998).

3.4. Basin Asymmetry Factor

The asymmetry factor (A_f) is used to measure the areal drainage basin asymmetry of the two sides of the main trunk (Hare and Gardner, 1985; Keller and Pinter, 2002):

$$A_f = 100.\left(\frac{A_r}{A_t}\right) \quad \text{Equation 2}$$

where A_r and A_t are the drainage areas, in map view, of the right river-side (A_r) and of the whole drainage basin (A_t), respectively. If a stream flows in the middle of its drainage basin, then A_f = 50 and the drainage basin is symmetrical. Therefore, A_f <50 and A_f >50 correspond to asymmetrical drainage basins, with a dominating left or right drainage area, respectively. A_f can be considered as a proxy of tectonic tilting perpendicular to the main-trunk channel direction (Hare and Gardner, 1985), although some lithologic control is also possible (El-Hamdouni et al., 2008).

3.5. Elongation ratio

Drainage basin shape, or elongation ratio (R_e), is defined as the ratio of the maximum width of a drainage basin (B_w) to its maximum length (B_l) (*e.g.,* Hurtrez, 1998):

$$R_e = \frac{B_w}{B_l} \quad \text{Equation 3}$$

To calculate the length of the watersheds, we measured the length of the centreline of the watershed. It is typically low for very elongated (elliptic) watersheds, which may be structurally controlled. On the contrary, circular basins (R_e ~ 1) are weakly influenced by structural or lithological parameters.

3.6. Normalized mean elevation

Elevation corresponds to the height of a landform relative to a datum. For each watershed, we calculate the basin average elevation that is normalized by subtracting the outlet elevation value. This allowed us to correct the watershed average elevation from the height of local base level height (*e.g.,* Ramsey et al., 2007; Hurtrez et al., 2011).

3.7. Local relief

Relief can be quantified in various ways (Hurtrez et al., 1999). In our study, we used in the definition of local relief (Ahnert, 1970) as a function of the length (Vergne and Souriau, 1993; Weissel et al., 1994), calculated at the scale of a drainage basin (Lucazeau and Hurtrez, 1997; Hurtrez et al., 1999). The local relief (Δz) is the average difference in elevation for a given length (Weissel et al., 1994; Hurtrez et al., 1999):

$$\Delta z(l) = < |z(x+l) - z(x)| > \quad \text{Equation 4}$$

where z is the elevation, l is the length scale, and x is the horizontal distance. The angle brackets indicate spatial averaging. Local relief provides some measures of the topographic roughness that is often controlled by climate changes and tectonic uplift rate at larger spatial scales, while rock type and geologic structures at smaller spatial scales (Chase, 1992; Rinaldo et al., 1995).

The behaviour of relief "*R*" with length scale "l" follows well the following power law relationship (Weissel et al., 1994):

$$R(l) = R_0 . l^H \quad \text{Equation 5}$$

where R_0 is the amplitude factor, defined as relief at a length scale of 1 km, and the scaling exponent H is the Hurst exponent. Equation 5 represents the roughness of the watershed topography and thus its sensitivity to erosion. In our study, we extracted the relief amplitudes at 0.2 km length scale, following Hurtrez et al. (1999).

3.8. Fluvial incision factor

Incision is the downcutting made by a vertical erosion. This is a geological process by hydraulic action that deepens the channel of a stream *(e.g.,* Lavé and Avouac, 2001; Brocard and van der Beek, 2006). The fluvial incision factor (If) quantifies incision in a valley by comparing the valley depth and width at a specific location:

$$I_f = 100.\left(\frac{L_R + L_l}{H}\right) \qquad \textbf{EQUATION 6}$$

where L_r and L_l are the right and left riverbank widths, respectively. H is the height between crestline and valley floor. In our work, we quantified the incision factor in each valley along the Qiulitage fold ridges following topographic profiles parallel to the fold strike and located at mid distance between the anticline crestline and the drainage basin outlet line.

3.9. Normalized steepness index

The channel slope (S) is linked to the drainage area (A) by an inverse power law as:

$$S = k_s.A^{-\theta} \qquad \textbf{EQUATION 7}$$

where k_s and θ correspond to the steepness index and concavity index, respectively (*e.g.,* Hack, 1957; Snyder et al., 2000). Channel longitudinal profiles and drainage areas were generated from 30 m resolution DEMs using ASTER program software. Then, power law regressions of channel slope as a function of drainage area were used to derive estimates of

channel concavity (θ) and steepness (k_s). To compare between drainage basins of different size, K_{sn} is often normalized steepness index (K_{sn}). The convex shape in a slope–area plot and a sudden rise of k_{sn} values along the streams are often interpreted as a transient river profile that is often caused by an increase in uplift rate (*e.g.,* Wobus et al., 2006; Whipple et al., 2013). The concavity index (θ) varies in channels between 0.4 and 0.6 under the influence of uplift rate, lithology and/or climate at steady states (*e.g.,* Wobus et al., 2006, Kirby and Whipple, 2012).

3.10. Hierarchical analysis

We analyzed the variability in morphometric indexes with a statistical approach that includes six parameters: basin area, normalized elevation, local relief, hypsometric integral, elongation ratio and asymmetry factor. It was carried out using the Ward method within the R software using the "h.clust" *(e.g.,* Ward, 1963). The aim of this hierarchical analysis is to divide a population (here, of drainage basins) into different classes. Items (*i.e.,* catchments) in each class should be as similar as possible, whereas classes should be as dissimilar as possible. We then represented the hierarchical analysis results in the form of a dendrogram, from which we choose a level of hierarchy that allows us to split watersheds into seven classes (numbered from 1 to 7, Fig. 10). The further apart the numbers, the greater the dissimilarity. For instance, drainage basins in class 1 are statistically very different from drainage basins in class 7. On contrary, class 1 and class 2 drainage basins are statistically closer. In addition, "boxplots" are used to represent the statistical distribution of morphometric data in each class (Fig. 10B). The upper bound of the box corresponds to the third quartile (75% of the values are below), whereas the lower bound corresponds to the first quartile (25% of the values are below). The

central bar gives the value of the median and the uppermost and lowermost dashed lines represent the extreme values.

4. Results

4.1. Topography and incision

Both the northern and southern ridges of the Southern Qiulitage, Kuqatawu and Misikantage anticlines are segmented with several domains of constant or increasing crestline elevation or incision values. This leads us to divide the fold belt into six morphostructures (MS1 to MS6), which are often separated either by water gaps or wind gaps (Fig. 3). Water gaps correspond to valleys that were carved during fold growth and that still host a flowing stream, whereas wind gaps constitute similar valleys that are presently dry and uplifted. Unfortunately, we cannot confirm whether the wind gaps preserve alluvial deposits, nor we cannot document whether transitions between adjacent morphostructures are controlled by structural features (fold tip, faults, etc.).

4.1.1. Southern ridge

From E to W, the crestline profile of the Southern Qiulitage ridge can be divided into three morphostructures: MS1, ~1600 m mean elevation (1978 m max. elevation), MS2 a western lower ridge (with 1400 m mean elevation), and MS3 a 1430 m mean elevated triangular landform (Fig. 3C, Table 2). MS1 and MS2 correspond to the Southern Qiulitage and Kuqatawu anticlines, respectively, whilst MS3 corresponds to the Misikantage anticline.

288 The crestline profile of MS1 displays a first order convex (or semi-elliptical) shape
289 (dashed purple line on Fig. 3C), which starts from Yanshui water gap to the east (at ~ 1500 m
290 in elevation), reaches a maximum elevation at the center of MS1 (~ 2000 m), and lowers to
291 1400 m at a major wind gap. Along MS2, elevation gradually increases westward from ~ 1500
292 to 1800 m. A major active water gap, associated with two narrow catchments draining the two
293 intermontane basins (WIB and EIB), cuts MS2 through a deep gorge. MS3 is a short (15-20 km
294 long) landform with a triangular plan-view profile (Figs. 1-C2 and 3).
295 The valley incision factor, calculated from the mid-flank profiles (yellow profiles, Fig. 3B),
296 displays large variations in amplitude. The limits between domains of constant incision and
297 domains of increasing/decreasing incision match quite well with the limits of the
298 morphostructures. For instance, the average incision for MS3 is extremely low (I*f* ~ 0.05),
299 whereas it increases to ~ 0.15 along MS2. In addition, the transition between MS2 and MS3
300 occurs at a change in trend of the incision curve. It displays a plateau in I*f* values of ~ 0.15 along
301 MS2 and then increases gradually until 0.25 within MS1. For MS1, the incision pattern is more
302 complex since our analysis proposes that it is divided into a western domain displaying a clear
303 eastward increase in incision values (I*f* from 0.05 to ~ 0.25), and a central-eastern domain
304 showing a gentle decrease in incision values (I*f* ~ 0.15). The highest incision value occurs close
305 to the transition between the domains of 1800 m and 2000 m constant crestline topography.

306 4.1.2. Northern ridge

307 The crestline profile of the Northern Qiulitage ridge can be divided in three
308 morphostructures (Fig. 3A): MS4, with profile showing a steady eastward decrease in
309 elevation, MS5 with an average crestline elevation of 1558 m, and MS6 with a long and

elevated crestline (1889 m) decreasing to 1400 m at the eastern wind gap. As MS1, the crestline profile of MS6 also displays a first order “semi-elliptical” shape (dashed purple line on Fig. 3A). The correspondence between morphostructures and anticlines is such that reflects MS4 relates well to Yakelike anticline, whilst MS5 and MS6 correspond to the Northern Qiulitage anticline.

The incision values along the northern Qiulitage ridge indicate a simple pattern that matches the morphostructures. MS4 presents low incision values decreasing slightly eastward (from 0.1 to 0.05). The lowest values of incision (at 0.05) fit the MS4/MS5 transition. Then, from MS5 to MS6, incision increases gradually eastward and reaches high values around 0.2-0.25. Toward the east, incision reduces sharply to 0.1. Remarkably, the valley incision record does not display a sharp change at the MS5/MS6 transition, neither within MS5. The crestline profile of MS5, with two topographic highs separated by a wind gap, is not associated with a particular pattern in the incision data. These observations drove us to consider that MS5 and MS6 may have a common morphostructural history related to the Northern Qiulitage anticline. Preserved wind gaps across MS4, MS5 and MS6 would reflect the location of former transverse channels that maintained their course through the anticlines during early fold growth, but which were finally defeated and forced to deviate.

4.2. Drainage network

The drainage network of the study area can be divided in two categories: 1) major rivers crossing the Qiulitage fold belt, which generate deep water gaps and are associated with large drainage basins and large alluvial fans, and 2) minor rivers developing from the fold belt topography (Fig. 5A). The first ones are perennial flows that drain rain and snow melt from

the upper part of the Tian Shan landforms, whereas the latter are intermittent channels that occasionally flow during local rainfall events and develop as debris flows.

4.2.1. Major cross-fold rivers

There are three major rivers that cross the Qiulitage fold belt and formed major water gaps or transverse gorges (Figs. 1, 3 and 4): from west to east, the Muzart-Weigan river system, and the Yanshui and Kuqa Rivers. Interestingly, they all cross the fold belt where topography consists of a single ridge, morphostructure MS1 of the Southern Qiulitage anticline. Water gaps (gorges) associated with these three rivers (Fig. 4B) display pronounced V-shaped valleys but also variations in bulk incision. Particularly, the topographic slopes of E- and W-facing hillslopes of the gorges are higher for the Weigan and Kuqa Rivers (about 20-28°) compared to the Yanshui River (average slope around 19-20°).

The drainage basins for these three rivers are remarkably different in terms of planar area (Fig. 4A). From the smallest to the largest, it varies from 300 km^2 for the Yanshui drainage basin, 2 960 km^2 for the Kuqa drainage basin and to 22 400 km^2 for the Weigan drainage basin. A two orders of magnitude difference in drainage basin area is observed between Weigan and Yanshui, although their water gap shapes are remarkably similar. This suggests that important changes in drainage basin areas have occurred in the past, likely due to drainage capture processes (see Discussion).

Several levels of fluvial terraces are preserved along the riverbanks of all these three rivers (Fig. 4C). Field observations of several of these terraces, notably in the Weigan and Yanshui watergap, indicate that they are mostly strath terraces capped by one to several

353 meters of alluvial deposits. They constitute important morphologic markers for further
354 measures and dating with the aim of unravelling the growth history of the Qiulitage anticlines.

355 4.2.2. Qiulitage drainage network

356 Most of the drainage network that developed across the Qiulitage fold belt consists of a
357 trellis-type pattern (Fig. 5A). The main longitudinal rivers are oriented ENE-WSW and develop
358 between the southern and northern anticlinal ridges, within the intermontane basins (WIB
359 and EIB). Both rivers flowing from the WIB and EIB coalesce and flow out of the fold through
360 a deep gorge. The area of this intermontane drainage basin is ~ 98 km^2.

361 A parallel drainage network is developed onto the northern flank of the NQA (MS6) and
362 onto the southern flank of the SQA (MS1). On the northern flank of the NQA, major transverse
363 rivers trend NW–SE, perpendicular to the fold axis, and cut deep V shaped valleys, as
364 documented from the mid-slope profile (Fig. 3). Locally, there are anomalous drainage
365 configurations (drainage deflection), notably for the northern flank of MS6. Dendritic drainage
366 networks are developed onto the southern flank of the SQA (MS2) with high headward erosion
367 (vertical river incision values of ~2 km) (Fig. 8C). Small catchments developed onto the
368 northern steep flanks of the SQA (MS1) and the southern steep flanks of the NQA (MS6),
369 exhibit a high-density dendritic drainage pattern.

370 ## 4.3. Morphometry of the Qiulitage watersheds

371 After presenting the drainage network developed on the fold ridges, we quantified the
372 morphometry of drainage basins, through several morphometric parameters, such as the
373 longitudinal stream profiles, basin area, basin slope, basin relief, hypsometry, basin
374 asymmetry, basin shape and K_{sn} (Figs. 5B and 6).

375 4.3.1. Drainage area

376 Most of the catchment areas are about 1.7 to 5 km^2 in size (average catchment area of
377 2.78 km^2, Table 2). The larger-sized catchments (13 to 26 km^2) are located on the northern
378 side of MS6 and southern side of MS2. In 75% of the investigated study area, watersheds are
379 small (1.5 to 5 km^2) and have a variable morphology (mostly elongated or sub-rounded).

380 4.3.2. Longitudinal stream profiles

381 The analysis of longitudinal stream profiles allows identification of localized breaks in
382 slope (knickpoint or knickzones) along the main trunk channel, suggesting disequilibrium. The
383 presence of knickpoints, combined with documented evidence for gorges and ridge anticlines
384 (Stokes et al,. 2008), can be explained as a result of transient fluvial incision across the region
385 (*i.e.,* Wobus et al., 2003; Whittaker et al., 2007 and 2008; Kirby and Whipple, 2012; Miller et
386 al., 2012). We explore the potential formation mechanisms of the knickpoints identified along
387 the KFTB and their tectonic implications.

388 One longitudinal stream developed onto the northern flank of the Northern Qiulitage
389 anticline has been investigated in detail (Figs. 5A and 7) based on remote sensing and field
390 observations. The stream presents two major convex segments (Fig. 7C) that correspond to
391 two sets of knickzones. In the upstream domain of the channel profile, very gentle channel
392 gradients of < 1% are associated with semi-closed, perched sub-horizontal depressions that
393 are partially filled with aeolian sands (labelled “2” in Fig. 7C). Downstream, we observed thick
394 (~ 5-10 m) laminated fill terrace deposits preserved along the main trunk (“1” and “3” in Fig.
395 7C.). The width of the channel also changes along the stream, being narrow upstream (5 m
396 wide), widening in the central part (40-50 m wide) and finally narrowing again (5-10 m wide)

(Fig. 7A). A major ~300 m-long knickzone is observed in the downstream part of the channel together with two local knickpoints anchored on resistant and thick sandstone layers. The upper knickpoint (K_u) (labelled "3" in Fig. 7C) is located at the downstream end of the wide channel segment (Fig. 7A). The lower knickpoint (K_l) marks the upstream end of the 300 m long knickzone and the downstream end of the thick-slope laminated deposits. These deposits are horizontal and non-deformed. They unconformably overlie the northward dipping Upper Miocene rocks of the Kangcun Formation. The unconformity surface represents a paleo-thalweg that could be interpreted as a terraced paleo-topographic surface.

Along MS2, the two rivers draining the WIB and EIB have been investigated in terms of the shape of their longitudinal profile and fluvial style (labelled "2" in Fig. 7D). Valley incision has been also calculated along the water gap and within the EIB, downstream of the confluence (labelled "3" in Fig. 7D). Both the WIB and EIB channels present flat gradients within upstream reaches where the river flows across the Quaternary alluvial plain to their confluence, the longitudinal profiles of the two rivers show a sharp increase in slope value (knickzone labelled "K_1"), which is accompanied by a change in fluvial style from braided to meandering channels (see section 4.3.2). Downstream of the confluence, another flat stream segment is observed before a major 5 km long knickzone (labelled "K_2"). K_2 is localized within the hanging wall of the E-W Southern Qiulitage back-thrust that breaks the hinge of the Southern Qiulitage anticline (labelled "3" in Fig. 7D).

4.3.3. Normalized steepness index (ksn)

For the Qiulitage drainage network, the lowest values ($k_{sn} < 50$) are observed for rivers flowing through the Tarim plain, Baicheng Basin and in the two longitudinal intermontane

419 basins (WIB and EIB). Contrastingly, rivers intersecting the anticlines and cutting through their
420 Cenozoic bedrock present the highest k_{sn} values. Indeed, the highest values (k_{sn} > 100-300) are
421 observed for rivers draining from the ridges. Steep rivers characterize the Kuqa and Kangcun
422 formations and the titled alluvial fan deposits at the toe of the Southern Qiulitage anticline
423 (Fig. 5B), where knickpoints exist. The concave-upward rivers also vary in k_{sn} values, ranging
424 from 25 to 300 (Fig. 5B). The majority of them flow across thrust faults and the steeply-dipping
425 northern and southern limbs of anticlinal ridges, as do the rivers with knickpoints.

426 4.3.4. Basin asymmetry

427 In plan-view, MS5 and MS6 show a pronounced asymmetry of drainage area on the
428 opposite limbs of the northern Qiulitage fold (Figs. 5A and 6A). Moderate-size catchments (2
429 to 4 km^2) are observed on the southern limb, whereas larger drainage basins (2 to 10 km^2) are
430 common on the northern limb. Similarly, MS1 shows an asymmetric anticline with a steep
431 northern limb and a gently dipping southern limb. Small-size catchments (2 to 4 km^2) are
432 observed for the northern limb whereas larger catchments (3 to 15 km^2) are observed for the
433 southern limb (Fig. 5A and B). On the northern limb, drainage basins are narrow, highly incised
434 and valley floors are steep (Figs. 3C and 6A; 25-30°).

435 Catchments are generally wider on the west-facing side than on the east-facing one (Fig.
436 9A). This asymmetric configuration is clear along the entire length of MS6 northern flank, and
437 it is particularly striking for the western drainage basins (Fig. 6E and labelled “a” and “b” in
438 Fig. 9A). Accordingly, drainage-average slopes are steeper for east-facing hillslopes (30°) than
439 for west-facing hillslopes (12 to 20°). In general, the slope values tend to decrease from west
440 to east (labelled “a” to “d” in Fig. 9A and D).

441 In MS6, the axis of the anticline is approximately N60°E. From west to east, the main
442 northward-flowing streams are oriented from N047 to N330, indicating an eastward decrease
443 in deflection. We noticed a systematic eastward deflection of the main trunks (Fig. 9B, C and
444 E). The two parameters (deflection and asymmetry) appear to be correlated (Fig. 9D). The
445 deflection decreases with the decreasing basin asymmetry. Meanwhile, we observed an
446 eastward decrease (4 to 2) in stream order as defined by Strahler (1952), and a decrease in
447 drainage density (ratio of the total length of streams in a watershed over its contributing area)
448 on MS6 (Fig. 9C). We interpret these variations as evidence for eastward fold propagation.
449 Similar correlations between fold lateral growth, drainage deflection and drainage network
450 asymmetry have been previously deciphered on other active folds, such as the Wheeler
451 anticline in California, the Pakuashan anticline in the Western Foothills of Taiwan or the
452 Marand anticline in the North-Tabriz Fault-Zone (NW Iran) (Mueller and Talling, 1997; Keller
453 et al., 1998; Delcaillau et al., 2006).

454 4.3.5. Local relief and normalized mean elevation

455 The highest values of local relief are observed in the western part of MS6 and the central
456 part of MS1 (red and orange), *i.e.,* $\Delta z_{(200m)}$=50-80 m and α =25-30°. Lowest values of local relief
457 are observed for MS3 (dark blue), *i.e.,* $\Delta z_{(200m)} < 20$ m and $\alpha < 10°$. MS5 displays also small
458 values of local relief ($10 \text{ m} < \Delta z_{(200m)} < 30$ m) and mean slope ($5° < \alpha < 15°$).

459 The computation of normalized mean elevation, gives rise to a similar trend to that of
460 local relief. The highest normalized elevations are measured for the central region of MS1
461 (z=400-550 m) and to a lower extent MS6 (z=300-400 m). MS3, MS4 and MS2 present

462 intermediate (z=100-400 m) values that are sometimes dissymmetric apart from the ridge
463 crestline (*e.g.,* for MS2).

464 4.3.6. Hypsometry

465 The analysis of hypsometric integrals in the northern and the southern flanks of
466 Qiulitage ridges shows significant differences along the structures (Fig. 6D, Table 2). Along
467 MS1, the hypsometric integral values are high on the southern flanks of the ridge (HI= ~0.5).
468 Some of the highest hypsometric integral values (HI >0.55) are observed along this ridge. Such
469 high values of HI, together with high incision values for those basins (Fig. 3), verify the intense
470 river incision stage of these parts of the folds. It suggests a sustained recent uplift of the
471 drainage basins and an active growth of the Southern Qiulitage fold, which is consistent with
472 the ~600- to 700-m-high triangular facets interpreted as indicator of an active uplift across the
473 hinge zone at the southern toe of the fold (Hubert-Ferrari et al., 2007). Hypsometric integrals
474 are also high for MS6 and MS3 (< 0.4 and < 0.6 respectively), but are lowest for MS2 and MS5
475 (< 0.3 and < 0.5 respectively). This suggests that both morphological structures MS2 and MS5
476 are less active than the others, which also agrees with the lower values of crestline topography
477 and valley incision (Fig. 3).

478 4.3.7. Elongation ratio

479 The pattern of the elongation ratio is not as clear as for other morphometric indexes
480 (Figs. 6F and 10). However, highly elongated drainage basins (in blue with low values of <0.3)
481 are mostly observed along the southern flank of the MS1 and the northern flanks of MS6 -
482 MS5. MS2 shows weakly elongated and smaller basins on its northern flanks (values = 0.6).
483 While MS3 presents a high proportion of weakly elongated basins (values < 0.4) on both flanks,

MS2 and MS4 present somewhat circular shapes. The correlations between basin area and elongation ratio are complex but they are good for MS4 (low drained area and low elongation), average for MS5, very good on the southern flank of MS6 (very low drained area and very low elongation), low for MS3, good for the western part of MS2 (low drainage area and low elongation), very good on the northern flank (very low drainage area and very low elongation), and good for the eastern part of the southern flank (low drainage area and low elongation) of MS1.

4.3.8. Morphometric synthesis

The map of statistical classes of basins (Fig. 10) highlights clearly the six morphological structures inferred from the topographic analyses (Fig. 3). Specifically, their limits match well. For instance, MS1 is the most clearly constrained and statistically homogeneous morphological structure, because it exposes mostly two classes all along its strike. In addition, it displays a clear separation between northern and southern limb catchments, where northern catchments belong to class 1, whilst southern catchments belong to class 2. Further east of the Weigan River water gap, drainage basins become more heterogeneous, and catchments belong to sets 4, 5, 6 and 7. MS2 displays catchments that are highly heterogeneous because of the seven classes of cluster observed. However, a trend can be distinguished because drainage basins belong mostly to classes 5 and 7. MS3 drainage basins are statistically very homogeneous since they essentially belong to class 3. MS4 is not sufficiently well constrained to be described, due to a lack of reliable drainage basin information. In contrast, MS5 and MS6 show quite homogeneous drainage basin statistics. The northern limb catchments belong dominantly to class 4, which suggests a genetic and

morphodynamic link between these two morphostructures. The eastern part of the MS6 is quite heterogeneous. This might be expected since this portion of the fold would express the connection between MS6 and MS5.

5. Discussion

5.1. Morphometry of the Qiulitage morphostructures

Based on our morphometric analysis of the Qiulitage topography, incision and watershed morphometry, we consider that both the southern and northern Qiulitage ridges can be divided into three morphostructural units. These are the eastern MS1, the central MS2 and the western MS3 units for the southern ridge, and the western MS4, the central MS5 and the eastern MS6 units for the northern ridge. These ridges collectively display contrasting morphometric values that we can consider to account for differentiated fold growth history.

For MS1, high and fairly constant elevation ($z \sim 1800$ m), high local relief ($R > 50$ m), high hypsometric integrals ($HI > 0.55$) and remarkably elongated basins (Figs. 3 and 6), would reflect a mature and actively uplifting morphological structure. This could mean that this landform may have reached locally a topographic steady state (Hubert-Ferrari et al., 2007). In addition, the high asymmetry of drainage basin area between the southern and northern flanks corroborates the northern vergence of the structure observed from field mapping and seismic interpretation.

For MS2, the slightly varying crestline elevation (1600 – 1700 m), low local relief ($R <$ 40 m), low hypsometric integrals ($HI < 0.5$) and weakly elongated basins (Figs. 3 and 6), would reflect a slightly uplifting structure. Similar values of slopes and areas along the two flanks of

the MS2 ridge do not decipher any specified vergence of the structure, as confirmed by the seismic profiles that image a symmetrical and tight anticline (Fig. 1). The transition between MS1 and MS2 coincides with a significantly low wind gap (elevation 1350 m) that we interpret to reflect a change in deformation accommodation along the Qiulitage fold belt.

For MS3, highly varying elevations (1500 – 1900 m), very low incision values (0.05) extremely low local relief (R< 20 m), but high hypsometric integrals (HI > 0.5) and very elongated basins (Figs. 3 and 6), suggest a very young and actively uplifting morphostructure. Considering the remarkable radial pattern of the drainage network, MS3 is likely controlled by a subsurface structure, such as an active salt diapir. The rapid uplift of MS3 could have integrated uplift of the western side of MS2, whose general topography is tilted eastward (Fig. 3). In the MS3 area, the lateral growth of folds is recorded by stream network morphology (He and Li, 2009). It is also suggested that the relative position and activity of basement faults, as well as the thickness of deep salt have a significant influence on the structural styles of the western Qiulitage fold belt (Chen et al., 2004; Tang et al., 2004; Yu et al., 2006). These folds are underlain by the accumulation of thick salt which locally exceeds 3000 m (Wang et al., 2011).

Along the northern Qiulitage ridge, which is characterized by the western MS4 unit, the central MS5 unit and the eastern MS6 unit, we did not observe any geomorphic anomalies for MS4 associated with Yakelike anticline. Indeed, we failed to extract reliable information on the drainage basins, and the few catchments we analyzed did not allow us to draw any significant interpretations. As for MS5 and MS6, they are both geologically linked to the Northern Qiulitage anticline. Our geomorphological analysis shows how different the northern

549 and southern flanks are. While the northern flanks display high altitudes (1700 - 1900 m),
550 medium local average relief (R = 30 m), medium-to-large hypsometric integrals (HI = 0.5) and
551 very elongated basin, the southern flanks display smaller drainage surfaces, higher local relief
552 and slightly elongated basins (Figs. 3 and 6, Table 2). Similarly, for MS1, the asymmetry of the
553 drainage basin area and average slopes clearly reflects a south-vergent subsurface structure.

554 ## 5.2. Partitioning and propagation of deformation

555 Correlation between the topography and incision values of both the northern and
556 southern Qiulitage ridges provides insight into the growth mechanisms of Qiulitage fold belt.
557 In the absence of reliable chronological control on the timing, we rely on geomorphic criteria
558 to predict the deformation sequence (Burbank et al., 1997). As along-strike changes are
559 pronounced for all the anticlines, thereby each of them could be the dominant structure
560 accommodating shortening, reflecting partitioning of tectonic deformation. This deformation
561 partitioning occurs between the western part where the Qiulitage fold-belt is composed in
562 two fault-propagation folds, and the eastern part with a single overlapping structure with a
563 northern vergence.

564 For instance, where MS6 and MS2 face one another, MS6 presents high elevation
565 (~1900 m) and high incision values (~ 0.2), whereas MS2 presents low elevation (~ 1600 m) and
566 low incision values (0.1-0.15) (Fig. 3). This suggests that at 82°E longitude, MS6 has
567 accommodated most of the shortening, whereas less shortening has been incorporated on
568 the southernmost MS2. In contrast, further east, MS6 presents low elevation (~ 1600 m) and
569 decreasing incision values (0.15-0.1), whereas MS1 presents high elevation (~ 1800 m) and
570 incision values (0.2-0.25). This suggests that deformation is partitioned between MS6 to the

north and MS1 to the south. Further east, shortening is solely consumed along MS1 (Southern Qiulitage), resulting in high crestline elevation and high incision values (0.25). Finally, toward the eastern end of our investigated area, deformation is partitioned between several structures that accommodate shortening. It is mainly MS1, since its relief is the highest, but also frontal Kuqa and Yakeng open anticlines (Fig. 1). This would explain why both elevation and incision decrease toward the Yanshui River.

In this study, we investigated the asymmetry factor of the Qiulitage drainage basins and noticed that these values were particularly high (> 60%) along the northern flank of MS6 (Figs. 5A and 9A). This large asymmetry is illustrated by the pattern of the stream networks, with major tributaries coming from the right bank (Figs. 5A and 9B and C). This arrangement occurs because the small tributaries perpendicular to the main streams concentrate their erosion more on the northwestern side of the valley than on the southeastern side (Fig. 9B). The asymmetry factors generally show a uniform trend and river channels are affected by lateral tilting of the anticline ridge to the east. This asymmetry of the valleys seems to be controlled by a recent uplift of the fold in its western part.

5.3. River reorganization due to active folding

In this work, we document a two order of magnitude difference in drainage basin area between Weigan and Yanshui (Fig. 4A) which contrasts with a less significant difference in water gap shape (Fig. 4B). Therefore, we hypothesize that important changes in drainage basin areas have occurred in response to fold growth, involving likely drainage capture processes. Particularly, a much larger drainage basin than the present one would be expected to explain the large water gap of the Yanshui River. The Yanshui drainage basin may have been reduced

in size due to the capture of a portion of its drainage area by the Weigan fluvial system. For now, field arguments are still missing, but we consider that terrace analysis (notably source provenance analysis) might contribute to test this hypothesis.

In our work, we have interpreted several saddles along the crestline profiles of the northern and southern Qiulitage ridges as wind gaps. We did not have the opportunity to collect field evidence confirming this hypothesis, such as alluvial deposits at the saddles, but we consider this hypothesis reasonable *(e.g.,* Hubert-Ferrari et al., 2007; Zhang et al., 2021). For some examples, wind gaps are clearly preserved features that attest to the lateral propagation and linkage of anticlines (Jackson et al., 1996; Mueller and Talling, 1997; Keller et al., 1998; Hetzel et al., 2004; Ramsey, et al., 2007; Malik et al., 2010; Seong et al., 2011). For Qiulitage, we presume that several of the main saddles could be former water gaps. Those paleo water gaps would therefore evidence the paleo flow of ancient rivers across much younger and weakly elevated topographic ridges along the emerging Qiulitage fold belt. The Yakeng anticline (Hubert-Ferrari et al., 2007; Saint-Carlier et al., 2016; Zhang et al., 2021), south of the eastern Qiulitage anticline, could represent an analogue of what the early Qiulitage fold belt would have resembled. That is, a shallow anticline rising slightly above the regional datum which is traversed and gradually incised by several channels flowing from the upstream relief. Some channels may have enough stream power and discharge to maintain their course across the rising fold, but the others would be defeated and obliged to deviate. In addition, the appearance of a sinuous fluvial pattern for rivers flowing through the growing fold reflects a fluvial readjustment of the riverbed to an increase in the average slope linked

to the uplift of the central part of the Northern and Southern Qiulitage anticlines (MS2 and MS6) (Fig. 7D) (Schumm, 1993).

5.4. Fluvial terrace and alluvial fan deposits

On the northern flank of the Northern Qiulitage anticline, we interpret fluvial fill terrace deposits as an indicator of strong incision of the valley due to a recent uplift and locally a lithological control (Fig. 7A, B and C). Indeed, the presence of a major ~300 m long knickzone immediately southward of the preserved fill-cut deposits might indicate that the channel underwent a transient response to a perturbation where the knickpoint propagated upstream. However, the two knickpoints anchored on indurated sandstone layers would have blocked the upstream progression of the uplift instability and forced the channel to maintain a gentle slope upstream. The base of the thick slope-laminated deposits would correspond to a paleo-thalweg that has been incised. The terminal valley is characterized by aggradational fill terraces whose filling was controlled by base-level fluctuations. The filling of the terrace was dependent on the paleo-thalweg profile (Fig. 7B and C), and on the widening of the valley segments between the monoclines composed of indurated sandstone layers (Fig. 7A and C).

On the northern edge of the Northern Qiulitage anticline, several fill-cut terraces and strath terraces were identified in the field and from satellite images. For instance, three major surfaces (T1, T2 and T3) were observed on the upstream eastern part of the Yanshui gorge (Figs. 1 and 11A; Zhang, 2016) and one single terrace was observed on its upstream right bank (Figs. 1 and 11B). These terrace deposits are folded and faulted (Fig. 12A) or tilted northward (Fig. 11B).

On the southern edge of the SQA, large fossil alluvial fans, with truncated apices, have also been identified at the outlet of drainage basins along MS1 southern flank. These alluvial fans are mainly composed of two surfaces, Qf2 and Qf1, from youngest to oldest (Fig. 12). We observed that the recent (likely Holocene) incision was as large as ~100 m (Fig. 12A and E) at the outlet of the drainage basins. As the rivers were deeply incised into the piedmont, a large amount of material would have been removed to feed the modern fans (Qh) (Fig. 12A). Interestingly, the apices of Qf1 are still connected to the ridge front that coincides with the active axial surface of the fold (Fig. 12C and D) (Hubert-Ferrari et al., 2007). Since the oldest fans (Qf1) do not seem to be tilted basinward at the foot of the triangular facets, and that the segmented fan deposits gradually and systematically thin from the front to the piedmont plain, this could indicate that large incision is likely controlled by a local moderate uplift of the southern flank of the SQA.

5.5. Morphotectonic evolution of the Qiulitage fold belt

Here, we propose a planar morphostructural evolution of Qiulitage fold belt (Fig. 13) and provide some key 3D morphotectonic diagrams (Fig. 14) that account for a likely landscape evolution in the Kuqa Basin. These sketches integrate the results of previous studies (Hubert-Ferrari et al., 2007; Izquierdo-LLavall et al., 2018; Pla, 2019) and our morphometrics analyses. We propose a simultaneous evolution of the relief and drainage network. Ages for the different steps of this morphostructural story are based on published magnetostratigraphic dating of strata (*e.g.,* Charreau et al., 2020), and their kinematic relationships (pre-, syn- and post-tectonics) constrained from seismic investigations (*e.g.,* Izquierdo-LLavall et al., 2018).

Several factors exert a first order control on the geometry and kinematic evolution of the Kuqa fold-and-thrust belt: (1) the distribution of the two *décollements* in the Meso-Cenozoic sequence (*i.e.,* the Eocene-Oligocene and Miocene salt layers) and notably the position of salt pinch-out, (2) the reactivation of deep inherited structures, and 3) the changes in shortening amount accommodated within the fold belt. The change in syntectonic sedimentation rate across Kuqa Basin is also another factor that may have played a role in controlling this evolution, but we discarded it due to a lack of data for now.

5.5.1. Late Miocene (6-5 Ma)

The initiation of the Qiulitage fold belt started during late Miocene times (Kangcun-Kuqa Fm transition, *i.e.,* 6-5 Ma) (Figs. 13A and 14A) according to several studies based on structural geology, magnetostratigraphy, shortening analysis and growth-strata analysis (*i.e.,* Wang et al., 2011, Li et al., 2012, Tang et al., 2017; Tian et al., 2016; Charreau et al., 2020). As the initiation of deformation along the Kuqa Basin is generally considered to start around 20-25 Ma (Wang et al., 2011; Li et al., 2012), deformation was primarily accommodated along more hinterland structures like the Tuzimaza, Kumugeliemu and Suweiyi anticlines. Those structures are therefore thought to have accommodated shortening along the reactivated hinterland of the Tian Shan about 15-20 Ma before deformation propagated significantly basin-ward by 50-75 km. Surprisingly, the Qiulitage and Yakeng folds present approximately simultaneous ages of initiation around 6-5 Ma (Hubert-Ferrari et al., 2007), although their finite structures and morphologies are remarkably different. Both probably nucleated as blind structures, meaning that sedimentation rates were higher than uplift rates.

677 The position and strike (N70°E) of the Qiulitage ridge appears to be related to the
678 external limit (pinch-out) of the Kumugeliemu evaporite layer, which is presumably itself
679 controlled by an Oligocene extensional basin (Izquierdo-Llavall et al., 2018) (Fig. 14A). This
680 extensional basin, that developed whilst the Tian Shan was experiencing thrusting and folding,
681 would represent a local extensional stress regime along the foreland-basin forebulge. Cross-
682 section restoration and balancing suggest that the Qiulitage structures started folding by limb
683 rotation (Izquierdo-Llavall et al., 2018). The Paleogene Kumugeliemu evaporitic *décollement*
684 was activated and allowed deformation to propagate toward the distal pinch-out of the
685 viscous layer and to be concentrated along the Qiulitage fold belt. The subsalt geometry, and
686 particularly the high-angle normal faults bounding the small graben centred beneath the
687 Qiulitage fold belt (Izquierdo-Llavall et al., 2018), controlled the growth of Qiulitage (Fig. 14A).
688 North of Qiulitage, the Baicheng Basin became progressively a transported piggy-back
689 basin (*e.g.,* Beer et al., 1990; Talling et al., 1995), and it can be considered as active wedge-
690 top accumulations because completely contiguous with the foreland basin (De Celles et Giles,
691 1996).

692 5.5.2. Early to late Pliocene (5 – 2.6 Ma)

693 From the early to late Pliocene (*i.e.,* 5-2.5 Ma), while the syntectonic Kuqa Formation
694 was deposited in the foreland, the Qiulitage anticline (western, central and eastern segments)
695 probably emerged as a topographic ridge (Fig. 13B). Simultaneously, the Northern Qiulitage
696 anticline (Izquierd-Llavall et al., 2018) and the Misikantage anticline (Tang et al., 2017) are
697 thought to have nucleated, presumably as a buried feature first. The topographic emergence
698 of Qiulitage was made possible only when the uplift rate surpassed the sedimentation rate.

699 Based on magnetostratigraphy, sedimentation rates in the foreland were quite low during
700 early Miocene, and shortening and uplift of the Kuqa fold-and-thrust belt rates have probably
701 increased during the late Miocene to Pleistocene (Pla, 2019). Early thrusting conjugated to
702 detachment folding (Izquierdo-Llavall et al., 2018) could have contributed to accelerate uplift
703 and favor topographic emergence of Qiulitage. (Fig. 13B). We presume that the Yakelike and
704 Northern Qiulitage anticlines also nucleated during that period. As the early Southern
705 Qiulitage topographic ridge emerge, it started to affect the alluvial plain drainage and its
706 associated sedimentation patterns. The drainage response is expected to create antecedent
707 rivers across the emerging anticline. Most rivers were probably not diverted by anticlinal
708 ridges during fold uplift, meaning that the fluvial incision rate was higher than the uplift rate.

709 5.5.3. Early Pleistocene (2.5 Ma)

710 During Early Pleistocene times (*i.e.,* 2.5 Ma) (Fig. 13C), a twofold increase in shortening
711 rate is documented (Li et al., 2012; Charreau et al., 2020), which has likely accelerated the
712 topographic growth of the Southern Qiulitage anticline, as well as the topographic emergence
713 of the Northern Qiulitage and Yakelike anticlines. Thrusting, either blind or emergent, is
714 expected to occur simultaneously with folding. The backward propagation of deformation
715 from the Southern to the Northern Qiulitage is expected because deformation initially
716 nucleated at the external pinch-out of the basal Kumugeliemu *décollement.* Consequently,
717 deformation could not further propagate outward, but was forced instead to propagate
718 backward, in the so-called “out-of-sequence” mode. Several analogue models have
719 demonstrated this typical pattern of deformation propagation mode when deformation
720 reached the distal pinch-out of a viscous silicone polymer (Costa and Vendeville, 2002;

721 Graveleau et al., 2012). The topographic emergence of the Yakelike and Northern Qiulitage
722 folds, their growth and lateral propagation are expected to have deflected river streams
723 crossing Southern Qiulitage ridge. Paleo channels dating from the time when the Yakelike and
724 Northern Qiulitage anticlines were not emergent may have evolved toward water gaps and
725 later toward wind gaps under the influence of fold uplift. Wind gaps between MS6 and MS1
726 on one hand, and between MS4 and MS5 on the other hand, would represent topographic
727 evidence of this early segmentation of Qiulitage fold and their latter linkage.

728 5.5.4. Early to Middle Pleistocene (2-1 Ma)

729 From the Early to Middle Pleistocene (*i.e.,* 2-1 Ma) (Fig. 13D), the Qiulitage Northern
730 anticline propagated predominantly eastward, which led to the formation of the Quaternary
731 Intermontane Basin (EIB and WIB). This lateral propagation of the Northern Qiulitage anticline
732 (MS6) is recorded by the deflection pattern of the MS6 northern flank drainage (Fig. 9C and E)
733 and it would account for the partitioning of deformation between MS6 and MS1/MS2
734 recorded in the ridge topography and highlighted by the MS1/MS2 wind gap. Simultaneously,
735 we would expect that the Muzard River could have been captured by the Weigan River due to
736 the closure of the water gap between the Yakelike and Northern Qiulitage folds. Paleo-water
737 gaps of the Muzard river across the Southern Qiulitage fold would have evolved toward a
738 minor river draining solely the two intermontane basins.

739 5.5.5. Late Pleistocene to Present (0.5 to 0 Ma)

740 From the Late Pleistocene to the Present (0.5 to 0 Ma) (Figs. 13E and 14B), the Qiulitage
741 frontal structure continued to grow accommodating laterally the shortening that was
742 transferred from pre-salt structures. Another significant increase in shortening rate is

743 documented (Hubert-Ferrari et al., 2007; Wang et al., 2011; Tian et al., 2016), which is
744 expected to have affected the structural evolution of the Qiulitage fold belt, and therefore its
745 morphological evolution. This should have entailed accelerated uplift along Qiulitage and
746 likely incision of cross-fold rivers. This favors the abandonment of alluvial terraces across the
747 water gaps, as evidenced in the field (Fig. 4). Towards the Tarim Basin, the topographic
748 emergence of the Yakeng anticline would be dated to 0.2-0.3 Ma (Wang et al., 2011; Hubert
749 Ferrari et al., 2007).

750 6. Conclusion

751 The present morphological investigation of Qiulitage fold-belt in southern Tian Shan is
752 based on the analysis of 30 m DEMs and field observations. The topography, the incision
753 amount, and drainage networks have been analyzed for both the northern and southern
754 Qiulitage ridges. Six morphometric indices were computed at the scale of the 250 extracted
755 drainage basins and they were statistically confronted to analyze the geomorphological
756 response of Qiulitage landforms to fold uplift and lateral propagation of deformation. Results
757 propose the subdivision of the Qiulitage fold belt into six morphostructures (MS1 to MS6),
758 whose morphometric parameters provide good indicators of lateral propagation of folding
759 and partitioning of deformation within the fold belt. The observed drainage anomalies
760 (drainage network, knickpoints, wind gaps) are interpreted as a record of differential uplift
761 along the fold ridges. A geomorphic evolution model of the Qiulitage fold-belt is proposed and
762 integrates the influence of *décollement* geometry, deep inherited structures and changes in
763 shortening consumed in the fold-and-thrust belt. This model explains the suggested changes
764 in drainage basin areas, particularly between Yanshui and Weigan rivers, and interprets

765 observed wind gaps and water gaps as indicators of drainage capture processes and defeated
766 rivers diverted by fold growth.
767
768 **Acknowledgements** - We thank late Jean-Emmanuel Hurtrez for discussions about local
769 relief and for providing his GMT scripts to create figures at the early stage. We are grateful to
770 the editor (Dr. Martin Stokes) and anonymous reviewers for their constructive suggestions.
771 This work was supported by the TelluS-SYSTER Program of CNRS/INSU. The PHC Xu-Guangqi
772 program from the French and Chinese embassies is highly appreciated, supporting our
773 cooperation.
774

775 7. References

776 Abdrakhmatov, K.Y., 1996. Relatively recent construction of the Tien Shan inferred from
777 GPS measurements of present-day crustal deformation rates. Nature, 384, 450-453.
778 Ahnert, F., 1970. Functional relationships between denudation, relief, and uplift in large
779 midlatitude drainage basins. American Journal of Science, v. 268, p. 243-263.
780 Amos, C. B., Burbank, D.W., Read, S. 2010. Along-strike growth of the Ostler fault, New
781 Zealand: Consequences for drainage deflection above active thrusts. Tectonics, 29, TC4021,
782 doi:10.1029/ 2009TC002613.
783 Avouac, J.P., Tapponnier, P., Bai, M., You, H., Wang, G., 1993. Active thrusting and
784 folding along the northern Tien Shan and late Cenozoic rotation of the Tarim relative to
785 Dzungaria and Kazakhstan. J. Geophys. Res. Solid Earth, 98, 675-6804.

786 Bahrami, S., Capolongo, D., Rahdan-Mofrad, M., 2020. Morphometry of drainage basins
787 and stream networks as an indicator of active fold growth (Gorm anticline, Fars Province, Iran).
788 Geomorphology 355, 107086. https://doi.org/10.1016/j
789 Beer, J.A., Allmendinger, R.W., Figueroa, D.E. and Jordan, T.E., 1990. Seismic stratigraphy
790 of a Neogene piggyback Seismic stratigraphy of a Neogene piggyback, Argentian. Bull. Am. Ass.
791 petrol. Geol., 74, 1183–1202.
792 Bennett, E.R., Youngson, J.H., Jackson, J.A., Norris, R.J., Raisbeck, G.M., Yiou, F., Fielding,
793 E., 2005. Growth of South Rough Ridge, Central Otago, New Zealand: Using in situ cosmogenic
794 isotopes and geomorphology to study an active, blind reverse fault, J. Geophys. Res., 110,
795 B02404, doi: 10.1029/2004JB003184.
796 Bonnet, S., 2009. Shrinking and splitting of drainage basins in orogenic landscapes from
797 the migration of the main drainage divide. Nature Geoscience 2(11): 766-771.
798 Boulton, S.J., Stokes, M., Mather, A.E., 2014. Transient fluvial incision as an indicator of
799 active faulting and Plio-Quaternary uplift of the Moroccan High Atlas. Tectonophysics, 633,
800 16-33.
801 Bretis, B., Bart N., Grasemann B., 2011. Lateral fold growth and linkage in the Zagros fold
802 and thrust belt (Kurdistan, NE Iraq). Basin Research, v. 23, p. 615-630.
803 Brocard, G., Van der Beek, P.A., 2006. Influence of incision rate, rock strength, and
804 bedload supply on bedrock river gradients and valley-flat widths: Field-based evidence and
805 calibrations from western Alpine rivers (southeast France) In: Willett, S.D., Hovius, N.,
806 Brandon, M.T., and Fisher, D. Tectonics, Climate, and Landscape Evolution, Geological Society

of America, pp.101-126, Geological Society of America Special Paper 398, 10.1130/2006.2398(07).

Bull, W. B., 2009. Tectonically Active Landscapes: Wiley-Blackwell, pp. 326.

Bull, W.B., McFadden, L.D., 1977. Tectonic geomorphology north and south of the Garlock Fault, California. Geomorphology in Arid Regions, Proceedings of Eighth Annual Geomorphology Symposium. D. O. Doehring. State University of New York, Binghamton, 115-138.

Burbank, D.W., Anderson, R.S. 2011. Tectonic Geomorphology. Wiley-Blackwell; 2nd Edition.

Burchfiel, B., Brown, E., Qidong, D., Xianyue, F., Jun, L., Molnar, P., Jianbang, S., Zhangming, W., Huichuan, Y., 1999. Crustal shortening on the margins of the Tien Shan, Xinjiang, China. Int. Geol. Rev., 41, 665-700.

Charreau, J., Chen, Y., Gilder, S., Dominguez, S., Avouac, J.P., Sen, S., Sun, D., Li, Y., Wang, W.M., 2005. Magnetostratigraphy and rock magnetism of the Neogene Kuitun He section (northwest China): implications for Late Cenozoic uplift of the Tianshan mountains. Earth Planet. Sci. Lett. 230, 177-192.

Charreau, J., A. Sartégou, D. Saint-Carlier, J. Lavé, P.-H. Blard, S. Dominguez, S. L. Wang, G. Rao and A. Team, 2020. Late Miocene to Quaternary slip history across the Qiulitag anticline in the southern Tianshan piedmont. Terra Nova, 32(1): 89-96.

Chase, C., 1992. Fluvial land sculpting and the fractal dimension of topography. Geomorphology, 5, 39-57.

828 Chen, S.P., Tang, L.J., Jin, Z.J., Jia, C.Z., Pi, X.J., 2004. Thrust and fold tectonics and the
829 role of evaporates in deformation in the western Kuqa foreland of Tarim basin, northwest
830 China. Mar. Pet. Geol., 21, 1027-1042.
831 Cheng, K.-Y., J.-H. Hung, H.-C. Chang, H. Tsai and Q.-C. Sung, 2012. Scale independence
832 of basin hypsometry and steady state topography. Geomorphology, 171-172: 1-11.
833 Ciccacci, S., D'Alessandro, L., Fredi, P., Lupia-Palmeri, E., 1992. Relations between
834 morphometric characteristics and denudational processes in some drainage basins of Italy.
835 Zeitschfirt für Geomorphologie, 36, 53-67.
836 Collignon, M., Yamato, P., Castelltort, S., Kaus, B. J. P., 2016. Modeling of wind gap
837 formation and development of sedimentary basins during fold growth: application to the
838 Zagros Fold Belt, Iran, Earth Surf. Proc. Land., 41, 1521–1535.
839 Costa, E., Vendeville, B.C., 2002. Experimental insights on the geometry and kinematics
840 of fold-and-thrust belts above a weak, viscous evaporite décollement. Journal of Structural
841 Geology, 24:11, 1729-1739.
842 DeCelles, G., Giles, K. N., 1996. Foreland basin systems. Basin Research, 8, 105-123.
843 Delcaillau, B., Deffontaines, B., Floissac, L., Angelier, J., Deramond, J., Souquet, P., Chu,
844 H.T., Lee, J.F, 1998. Morphotectonic evidence from lateral propagation of an active frontal
845 fold: Pakuashan anticline, foothills of Taiwan, Geomorphology, 24(4), 263–290, doi:
846 10.1016/S0169-555X (98)00020-8.
847 Delcaillau, B., Carozza, J.M., Laville, E., 2006. Recent fold growth and drainage
848 development: the Janauri and Chandigarh anticlines in the Siwalik foothills, Northwest India,
849 Geomorphology, 76, 241-256.

Dolan, J.F., Avouac, J.P., 2007. Introduction to special section: Active Fault-Related Folding: Structural Evolution, Geomorphologic Expression, Paleoseismology, and Seismic Hazards. J. Geophys. Res., 112, B03S01, doi:10.1029/2007JB004952.

Doornkamp, J.C., King, C.A.M., 1971. Numerical Analysis in Geomorphology: an introduction, 372 pp. Londres, Ed.

El-Hamdouni, R., Irigaray, C., Fernández, T., Chacón, J., Keller, E.A., 2008. Assessment of relative active tectonics, southwest border of the Sierra Nevada (southern Spain). Geomorphology, 96, 150-173.

Gao, L., Rao, G., Tang, P., Qiu, J., Peng, Z., Pei, Y., Yu, Y., Zhao, B., Wang, R., 2020. Structural development at the leading edge of the salt-bearing Kuqa fold-and-thrust belt, southern Tian Shan, NW China. J. Struct. Geol. 140, https://doi.org/10.1016/j.jsg.2020.104184.

Giampaoli, P., Rojas Vera, E., 2018. Fold growth and lateral linkage in the southern Sub-Andean fold-and-thrust belt of Argentina and Bolivia. In: Zamora, G., McClay, K.R., Ramos, V.A. (Eds.), Petroleum Basins and Hydrocarbon Potential of the Andes of Peru and Bolivia: AAPG Memoir. 117, pp. 543-564.

Graveleau, F., Malavieille, J., Dominguez, S., 2012. Experimental modelling of orogenic wedges: A review, Tectonophysics, 538, 1-66.

Guerit, L., Barrier, L., Jolivet, M., Fu, B., Métivier, F., 2016. Denudation intensity and control in the Chinese Tian Shan: new constraints from mass balance on catchment-alluvial fan systems. Earth Surface Processes and Landforms, 41(8), 1088-1106. doi:10.1002/esp.3890

871 Hack, J.T., 1957. Studies on longitudinal stream profiles in Virginia and Maryland. U. S.
872 Geol. Surv. Prof. Pap., 294-B, 97.
873 Hare, P.W. and Gardner, T.W., 1985. Geomorphic Indicators of Vertical Neotectonism
874 along Converging Plate Margins, Nicoya Peninsula Costa Rica. In: Morisawa, M. and Hack, J.T.,
875 Eds., Tectonic Geomorphology. Proceedings of the 15th Annual Binghamton Geomorphology
876 Symposium, Allen and Unwin, Boston, 123-134.
877 He, D.J., Li, J., 2009. Drainage network development and fold growth of Quilitage
878 structural belt in the Kuqa foreland fold and thrust belt. Acta Geologica Sinica, 83, 1074-1082.
879 Hendrix, M.S., Dumitru, T.A., Graham, S.A., 1994. Late Oligocene-early Miocene
880 unroofing in the Chinese Tian Shan: an early effect of the India-Asia collision. Geology, 22, 487-
881 490.
882 Hetzel, R., Tao, M.X., Stokes, S., Niedermann, S., Ivy-Ochs, S., Gao, B., Strecker, M.R.,
883 Kubik, P.W., 2004. Late Pleistocene/Holocene slip rate of the Zhangye thrust (Qilian Shan,
884 China) and implications for the active growth of the northeastern Tibetan Plateau: Tectonics,
885 23, 6, TC6006, doi: 10.1029/2004TC001653.
886 Hubert-Ferrari, A., Suppe, J., Gonzalez-Mieres, R., Wang, X., 2007. Mechanisms of active
887 folding of the landscape (southern Tian Shan, China), J. Geophys. Res., 112, B03S09, doi:
888 10.1029/2006JB004362.
889 Hurtrez, J.E., 1998. Analyse géomorphologique des interactions tectonique-érosion dans
890 le système himalayen. ISTEEM, Université des Sciences et Techniques Montpellier II, PhD, pp.
891 203.

892 Hurtrez, J.E., Lucazeau, F., Lavé, J., Avouac, J.P., 1999. Investigation of the relationships
893 between basin morphology, tectonic uplift, and denudation from the study of an active fold
894 belt in the Siwalik Hills, central Nepal, J. Geophys. Res., 104 (B6), 12, 779-12,796.
895 Izquierdo-Llavall, E., Roca, E., Xie, H., Pla, O., Muñoz, J.A., Rowan, M. G., et al., 2018.
896 Influence of overlapping décollements, syntectonic sedimentation, and structural inheritance
897 in the evolution of a contractional system: The central Kuqa fold-and-thrust belt (Tian Shan
898 Mountains, NW China). Tectonics, 37(8), 2608-2632.
899 Jackson, J., Norris, R., Youngson, J., 1996. The structural evolution of active fault and fold
900 systems in central Otago, New Zealand: Evidence revealed by drainage patterns. J. Struct.
901 Geol., 18, 217–234.
902 Jackson, J., Van Dissen, R., Berryman, K., 1998. Tilting of active folds and faults in the
903 Manawatu region, New Zealand: evidence from surface drainage patterns, New Zealand.
904 Journal of Geology and Geophysics, 41, 377-385.
905 Jackson, J., Priestley, K., Allen, M., Berberian, M., 2002. Active tectonics of the South
906 Caspian Basin. Geophysics Journal International, 148, 214-245, doi:10.1046/j.1365-
907 246X.2002.01588.
908 Jin, Z., Yang, M., Lu, X., Sun, D., b, Tang, X., Peng, G., Lei, G., 2008.The tectonics and
909 petroleum system of the Qiulitagh fold and thrust belt, northern Tarim basin, NW China.
910 Marine and Petroleum Geology, 25, 767-777 Doi:10.1016/j.marpetgeo.2008.01.011.
911 Jolivet, M., Dominguez, S., Charreau, J., Chen, Y., Li, Y., Wang, Q., 2010. Mesozoic and
912 Cenozoic tectonic history of the Central Chinese Tian Shan: Reactivated tectonic structures
913 and active deformation. Tectonics 29, TC6019, doi:10.1029/2010TC002712.

914 Keller, E.A., Zepeda, R.L., Rockwell, T.K., Ku, T.L., Dinklage, W. S., 1998. Active tectonics
915 at Wheeler Ridge, southern San Joaquin Valley, California. Geol. Soc. of Amer. Bull. 110, 3:
916 298-310.
917 Keller, E.A., Pinter, N., 2002. Active Tectonics, Earthquakes, Uplift and Landscape. 2nd
918 Edition, Prentice Hall, Upper Saddle River, 362 p.
919 Keller, E.A., DeVecchio, D.E., 2013. Tectonic geomorphology of active folding and
920 development of transverse drainages. In: Shroder, J., Owen, L.A. (Eds.), Treatise on
921 Geomorphology. Tectonic Geomorphology vol. 5. Academic Press, San Diego, CA, pp. 129-147.
922 Kirby E, Whipple K.X., 2012. Expression of active tectonics in erosional landscapes. J.
923 Struct. Geol. 44, 54-75.
924 Lavé, J., Avouac, J.-P., 2001. Fluvial incision and tectonic uplift across the Himalayas of
925 central Nepal, J. Geophys. Res., 106, 26,561–26,591 doi:10.1029/2001JB000359.
926 Lee, J., 2015, Reconstruction of ancestral drainage pattern in an internally draining
927 region, Fars Province, Iran: Geol. Mag., 152 (5), 830-843.
928 Li, S., Wang, X., Suppe, J., 2012. Compressional salt tectonics and synkinematic strata of
929 the western Kuqa foreland basin, southern Tian Shan, China. Basin Research, 23, 1-23.
930 Lucazeau, F., Hurtrez, J.E., 1997. Length the scale dependence of relief along the
931 southeastern border of Massif Central (France), Geophys. Res. Lett., 24, 1823-1826.
932 Malik, J.N., Shah, A.A., Sahoo, A.K., Puhan, B., Banerjee, C., Shinde, D.P., Juyal, N.,
933 Singhvi, A.K., Rath, S.K.., 2010. Active fault, fault growth and segment linkage along the Janauri
934 Anticline (frontal foreland fold), NW Himalaya, India. Tectonophysics, 483 (3-4), 327–343.

935 Métivier, F. Gaudemer, Y., 1997. Mass transfer between eastern Tien Shan and adjacent
936 basins (Central Asia): constraints on regional tectonics and topography, Geophys. J. Int., 128,
937 1–17.
938 Miller, S.R., Baldwin, S.L., Fitzgerald, P.G., 2012. Transient fluvial incision and active
939 surface uplift in the Woodlark Rift of eastern Papua New Guinea. Lithosphere, 4, 131-149.
940 Doi:10.1130/L135.1
941 Molnar, P., Tapponnier P., 1975. Cenozoic tectonics of Asia: Effects of a continental
942 collision. Science, 189, 419–426.
943 Morisawa, M., Hack, J.T., 1985. Tectonic Geomorphology, Allen and Unwin, Boston.
944 Mueller, K., Talling, P., 1997. Geomorphic evidence for tear faults accommodating
945 lateral propagation of an active fault-bend fold, Wheeler Ridge, California. J. Struct. Geol., 19,
946 397–411, doi: 10.1016/S0191-8141(96)00089-2.
947 Ohmori, H., 1993. Changes in the hypsometric curve through mountain building
948 resulting from concurrent tectonics and denudation. Geomorphology, 8: 263–277.
949 Pike, R.J., Wilson, S.E., 1971. Elevation-relief ratio hypsometric integral and geomorphic
950 area-altitude analysis. Geol. Soc. Am. Bull., 82, 1079-1084.
951 Pla, O., 2019. Salt tectonics in contractional fold belts, the Kuqa foreland basin and thrust
952 belt case (Tarim basin, China), PhD, Universitat de Barcelona, pp. 198.
953 Poisson, B., Avouac, J.P., 2004. Holocene hydrological changes inferred from alluvial
954 stream entrenchment in north Tian Shan (north-western China). J. Geol., 112, 231–249.

955 Qiu, J., Rao, G., Wang, X., Yang, D., & Xiao, L., 2019. Effects of fault slip distribution on
956 the geometry and kinematics of the southern Junggar fold-and-thrust belt, northern Tian
957 Shan. Tectonophysics, 722, https://doi.org/10.1016/j.tecto.2019.228209.
958 Ramsey, L.A., Walker, R.T., Jackson J., 2007. Fold evolution and drainage development
959 in the Zagros mountains of Fars province, SE Iran. Basin Res., 20, 23-48.
960 Rinaldo, A., Dietrich, W.E., Vogel, G.K., Rigon, R., Rodríguez-Iturb, I., 1995.
961 Geomorphological signatures of varying climate, Nature, 374, 632-636.
962 Saint Carlier, D., Charreau, J., Lavé, J., Blard, P.H., Dominguez, S., Avouac, J.P., Shengli,
963 W., ASTER Team et al., 2016. Major temporal variations in shortening rate absorbed along a
964 large active fold of the southeastern Tianshan piedmont (China). Earth and Planetary Science
965 Letters 434, 333–348 http://dx.doi.org/10.1016/j.epsl.2015.11.041
966 Schumm, S.A., 1977. The Fluvial System. Wiley-Interscience, New York, 338 p.
967 Schumm, S.A., 1993. River response to base level change: implications for sequence
968 stratigraphy. J. Geol., 101, 279-294.
969 Seong, Y. B., Kang, H. C., Ree, J. H., Choi, J. H., Lai, Z., Long, H., & Yoon, H. O., 2011.
970 Geomorphic constraints on active mountain growth by the lateral propagation of fault-related
971 folding: A case study on Yumu Shan, NE Tibet. Journal of Asian Earth Sciences, 41(2), 184-194.
972 https://doi.org/10.1016/j.jseaes.2011.01.015
973 Sissakian, V.K., Elias, Z., Al-Ansari, N., 2019. Deducing the lateral growth of anticlines
974 using drainage analysis and geomorphological features. Geotectonics, 53, 140-154.

975 Snyder, N.P., Whipple, K.X., Tucker, G.E., Merritts, D.J., 2000. Landscape response to
976 tectonic forcing: digital elevation model analysis of stream profiles in the Mendocino triple
977 junction region, northern California. GSA Bull. 112, 1250–1263.
978 Stokes, M., Mather, A.E., Belfoul, A. Farik, F., 2008. Active and passive tectonic controls
979 for transverse drainage and river gorge development in a collisional mountain belt (Dades
980 Gorges, High Atlas Mountains, Morocco), Geomorphology, 102, 2-20.
981 Strahler, A.N., 1952. Hypsometric (Area Altitude) Analysis of Erosional Topology.
982 Geological Society of America Bulletin, 1117-1142. http://dx.doi.org/10.1130/0016-7606.
983 Sun, J. M., Li, Y., Zhang, Z.Q., Fu, B.H., 2009. Magnetostratigraphic data on Neogene
984 growth folding in the foreland basin of the southern Tianshan Mountains. Geology, 37(11),
985 1051-1054.
986 Sun, J., Zhang, Z., 2009. Syntectonic growth strata and implications for late Cenozoic
987 tectonic uplift in the northern Tian Shan, China. Tectonophysics, 463, 60–68.
988 Suppe J., 1983. Geometry and kinematics of fault-bend folding. Am. J. Sci., 283, 684-721.
989 Suppe, J., Medwedeff, D.A., 1984. Fault-propagation folding. G. S. A. Abstract with
990 programs, p 670.
991 Talling, P.J., Lawton, T.F., Burbank, D.W., and Hobbs, R.S., 1995. Evolution of latest
992 Cretaceous–Eocene nonmarine deposystems in the Axhandle piggyback basin of central Utah:
993 Geological Soeciety of America Bulletin, 107, 297–315.
994 Tang, L.J., Jia, C.Z., Jin, Z.J., Chen, S.P., Pi, X.J., Xie, H.W. 2004. Salt tectonic evolution and
995 hydrocarbon accumulation of Kuqa foreland fold belt, Tarim Basin, NW China. J. Petrol. Sci.
996 Eng., 41, 97–108.

997 Tang, Z.H., Dong, X.X., Wang, X., Ding, Z.L., 2015. Oligocene-Miocene
998 magnetostratigraphy and magnetic anisotropy of the Baxbulak section from the Pamir-Tian
999 Shan convergence zone. Geochem. Geophys. Geosyst., 16, 3575–3592.
1000 Tang, P., Rao, G., Li, S., Yu, Y., Pei, Y., Wang, X., Shen, Z., Chen, N., Zhao, B., 2017. Lateral
1001 structural variations and drainage response along the Misikantage anticline in the western
1002 Kuqa fold-and-thrust belt, southern Tianshan, NW China. Tectonophysics, 721, 196– 210.
1003 Tapponnier, P., Molnar, P., 1979. Active faulting and Cenozoic tectonics of the Tien Shan,
1004 Mongolia, and Baykal regions. J. Geophys. Res., 84 (B7), 3425 – 3459.
1005 Tian, Z., Sun, J., Windley, B.F., Zhang, Z., Gong, Z., Lin, X., Xiao, W., 2016. Cenozoic
1006 detachment folding in the southern Tian shan foreland, NW China: Shortening distances and
1007 rates. Journal of Structural Geology, 84, 142–161. https://doi.org/10.1016/j.jsg.2016.01.007.
1008 Vergne, M., Souriau, M., 1993. Quantifying the transition a between tectonic trend and
1009 mesoscale texture in topographic data. Geophys. Res. Lett., 20, 2139-2141.
1010 Wang, X., Suppe, J., Guan, S., Hubert-Ferrari, A., Gonzales-Mieres, R., Jia, C., 2011.
1011 Cenozoic structure and tectonic evolution of the Kuqa fold belt, southern Tian Shan, China. In:
1012 McClay, K., Shaw, J.H., Suppe, J. (Eds.), Thrust Fault-related Folding. AAPG Memoir, 94, 215-
1013 243.
1014 Ward, J.H., 1963. Hierarchical grouping to optimize an objective function. J. Am. Stat.
1015 Assoc., 58 (301): 236-244.
1016 Weissel, J.K, Pratson, L.F, Malinverno, A., 1994. The length-scaling properties of
1017 topography. J Geophys. Res., 99, 13997-14012.

1018 Whipple, K.X., Dibiase, R.A., Crosby, B.T., 2013. Bedrock rivers. In: Treatise on
1019 Geomorphology, Schroder, J., Wohl, E. (eds). Academic Press, San Diego, CA; 550-573.
1020 Whittaker, A.C., Cowie, P.A., Attal, M., Tucker, G.E., and Roberts, G., 2007. Contrasting
1021 transient and steady-state rivers crossing active normal faults: new field observations from
1022 the Central Apennines, Italy. Basin Research, 19, 529-556.
1023 Whittaker, A.C., Attal, M., Cowie, P.A., Tucker, G.E., Roberts, G., 2008. Decoding
1024 temporal and spatial patterns of fault uplift using transient river long profiles.
1025 Geomorphology, 100, 506-526.
1026 Willemin, J.H., Knuepfer, P.L.K., 1994. Kinematics of arc-continent collision in the eastern
1027 Central Range of Taiwan inferred from geomorphic analysis. J. Geophys. Res., 20267-20280.
1028 Wobus, C.W., Hodges, K.V., Whipple, K.X., 2003. Has focused denudation sustained
1029 active thrusting at the Himalayan topographic front? Geology, 31, 861-864.
1030 Wobus, C., Whipple, K.X., Kirby, E., Snyder N., Johnson, J., Spyropolou, K., Crosby, B.T.,
1031 Sheehan, D., 2006. Tectonics from topography: procedures, promise, and pitfalls. Geological
1032 Society of America Special Papers, 398, 55 e 74. http://dx.doi.org/10.1130/2006.2398(04).
1033 Xu, C., Zhou, X.Y., 2007. Seismic interpretation of the Kelasu triangle zone in the
1034 southern Tian Shan foothills, northwestern China. AAPG Bulletin, 91(2), 161-171.
1035 Yang, S., Jie, L., Wang, Q., 2008. The deformation pattern and fault rate in the Tian Shan
1036 Mountains inferred from GPS observations. Science in China series D: Earth Sci., 51, 1064-
1037 1080.
1038 Yin, A., Nie, S., Craig, P., Harrison, T., Ryerson, F., Xianglin, Q., Geng, Y., 1998. Late
1039 Cenozoic tectonic evolution of the southern Chinese Tian Shan. Tectonics, 17, 1-27.

Yu, Y.X. 2006. The salt-related structures and their formation mechanisms in the Qiulitag structural belt, Kuqa depression. Doctorate of engineering paper, China University of Petroleum, Beijing, pp. 25–94 (in Chinese with English abstract).

Yu, S., Chen W., Evans, N.J., McInnes, B.I.A., Yin J., Sun Jingbo, Li J., Zhang B., 2014. Cenozoic uplift, exhumation and deformation in the north Kuqa Depression, China as constrained by (U–Th)/He thermochronometry. Tectonophysics, 630, 166-182.

Zhang, L., 2016. Late Quaternary shortening and deformation mechanism across the Kuqa fold-and-thrust belt on the south of the Tienshan Mountains, PhD Institute of Geology, China Earthquake Administration, 89 p.

Zhang L., Yang X., Huang W., 2021. Fold segment linkage and lateral propagation along the Qiulitage anticline, South Tianshan, NW China, Geomorphology, 381, https://doi.org/10.1016/j.geomorph.2021.107662.

Zhao, B., Wang, X., 2016. Evidence of early passive diapirism and tectonic evolution of salt structures in the western Kuqa depression (Quele area), southern Tianshan (NW China). J. Asian Earth Sci., 125, 138-151.

Zubovich, A.V., Wang, X.Q., Scherba, Y.G., Schelochkov, G.G., Reilinger, R., Reigber, C., Mosienko, O.I., Molnar, P., Michajljow, W., Makarov, V.I., Li, J., Kuzikov, S.I., Herring, T.A., Hamburger, M.W., Hager, B.H., Dang, Y.m., Bragin, V.D., Beisenbaev, R.T., et al., 2010. GPS velocity field for the Tien Shan and surrounding regions, Tectonics, 29, TC6014, doi:10.1029/2010TC002772.

Figure captions

Figure 1: (A) Topographic map of central Asia (topographic data from Nasa STRM V.4.0). (B) Geological map of the Qiulitage fold belt (modified after Wang et al., 2011). (C) Geological cross-sections (modified from Li et al., 2012; Pla, 2019). Location shown in (B). QSN: Quele Salt Nappe, NQT: Northern Qiulitage Thrust, SQT: Southern Qiulitage Thrust, NQA: Northern Qiulitage anticline, SQA: Southern Qiulitage anticline, EQA: Eastern Qiulitage anticline, WIB: Western Intermontane Basin, EIB: Eastern Intermontane Basin.

Figure 2: Stratigraphic column of sedimentary formations in Kuqa Basin (modified after Jin et al., 2008 and Li et al., 2012). Significant *décollements* are indicated: LD (Lower *Décollement*), MUD (Main Upper *Décollement*) and mUD (minor Upper *Décollement*) following Izquierdo-Llavall et al., 2018. Note change in vertical scale for the Mesozoic and Cenozoic strata.

Figure 3: Topography along the Northern and Southern Qiulitage anticlines with topographic profiles along the crestline as insets (A and C). B: topographic data from NASA-SRTM. Light blue traces correspond to crestline profiles and yellow traces correspond to mid-flank profiles from which fluvial incision factors (I_f) are computed. Topographic analysis allows subdivision of the fold belt into six first-order morphologic structures (MS1 to MS6). “WG” stands for “wind gap” and “wg” stands for “water gap”.

Figure 4: A) Present drainage basins of major rivers flowing across the Qiulitage fold belt. From west to east, these are intermontane rivers: the Weigan, Yanshui and Kuqa Rivers. Drainage basin areas are indicated. B) Google Earth image (CNES/Airbus/Maxar technologies/Landsat Copernicus) of the Weigan, Yanshui and Kuqa water gaps illustrating the

overall valley incision and riverbank average slope. C) Field photographs of terraces preserved across Weigan and Yanshui channels.

Figure 5: A) Drainage network of Qiulitage fold belt. Letters refer to stream profiles of Figures 7 and 9. B) Distribution of K_{sn} values along the Qiulitage fold belt.

Figure 6: Morphometric indices along the Qiulitage fold belt. A) Area, B) Normalized mean elevation, C) Local relief at 200m length scale, D) Hypsometric integral, E) Asymmetry factor and F) Elongation ratio.

Figure 7: A) Google Earth image (CNES/Airbus/Maxar technologies/Landsat Copernicus) along a channel (see location on Fig. 5 – blue label a) that develops on the northern flank of the Northern Qiulitage anticline. Channel width is bounded by white lines; yellow solid lines indicate the Late Pleistocene slope deposits; thick dark blue curves indicate the river profile knickzone. Inset #2 in the upper river valley represents the upstream depression. B) Field view of slope deposits preserved along the channel and C) associated channel longitudinal topographic profile and knickpoints. D) Google Earth image (CNES/Airbus/Maxar technologies/Landsat Copernicus) and stream profile and fluvial style in the Western and Eastern Intermontane Basins (WIB and EIB, respectively).

Figure 8: Google Earth images (CNES/Airbus/Maxar technologies/Landsat Copernicus) of channel network styles in A and C. A-B) Western Intermontane Basin (WIB) and C) Eastern Intermontane Basin (EIB). Relationships between alluvial fans deposits and bordering landforms are highlighted by black dotted lines. Blue dotted lines indicate headward erosion. NQA: Northern Qiulitage anticline; SQA: Southern Qiulitage anticline.

Figure 9: A) Transverse topographic profiles along the northern flank of the Northern Qiulitage anticline (location in Figure 5A) where the gradients of the east-facing and west-facing hillslopes are indicated. Grey inset represents the average trend of hillslope gradients for each profile. It indicates that drainage basin asymmetry tends to decrease eastward. B) Asymmetry map of drainage basins indicating the stream deflection lines. C) Spatial and temporal drainage network evolution from west to east of the northern limb of northern Qiulitage anticline. D) Correlation of asymmetry factors and drainage deflection with distance.

Figure 10: Statistical analysis of morphometric parameters of catchment basins using an ascending hierarchical analysis. (A) Map of the hierarchical groups, labelled 1 to 7. (B) Results of statistical analysis for six different metrics: area, normalized mean elevation, local relief at 200 m length scale, hypsometric integral, elongation ratio and valley asymmetry factor.

Figure 11: Evidence of active tectonic deformation along the northern flank of Southern Qiulitage anticline (see location on Figure 1B). A) Uplifted terraces and faulted fan deposits (Zhang, 2016). B and C) Tilted Pleistocene debris-flow-dominated alluvial fan deposits along the north verging Southern Qiulitage Thrust (SQT).

Figure 12: Google Earth image (CNES/Airbus/Maxar technologies/Landsat Copernicus) of alluvial fan entrenchment along the southern mountain front of Southern Qiulitage anticline. A-C) Quaternary (Qf1, Qf2) and Holocene (Qh) alluvial deposits are segmented and entrenched between triangular facets that dominate the topographic front. D-E) Incision larger than ~100 m has led to the entrenchment of fan deposits that do not appear folded across the active syncline axial surface.

1124 **Figure 13**: Morphotectonic evolution of central Qiulitage fold belt from A) Late Miocene
1125 to E) Present. See text for details.
1126 **Figure 14**: 3-D block diagram of A) the initial stage (during Late Miocene) and B) the
1127 present morphotectonics of central Qiulitage fold belt. Central Qiulitage fold belt formation
1128 appears primarily controlled by the distal pinch-out position of the Eocene evaporite basin,
1129 which was itself controlled by the presence of a deep Oligocene graben. This graben was
1130 tectonically inverted which triggered the evaporite inflation in Qiulitage fold core and its
1131 topographic growth. Sections 4, 5 and 6 in Fig.14A correspond to the names of sections in
1132 Figure 1. See text for details.
1133
1134 **Table 1**. Definition of morphometric parameters used in this study.
1135 **Table 2**. Average values of each morphometric parameter computed for the southern
1136 and northern flanks of the six morphostructures. Average of mean elevation and mean slope
1137 correspond to the spatial averaging (for each of mean values of each drainage basins).
1138

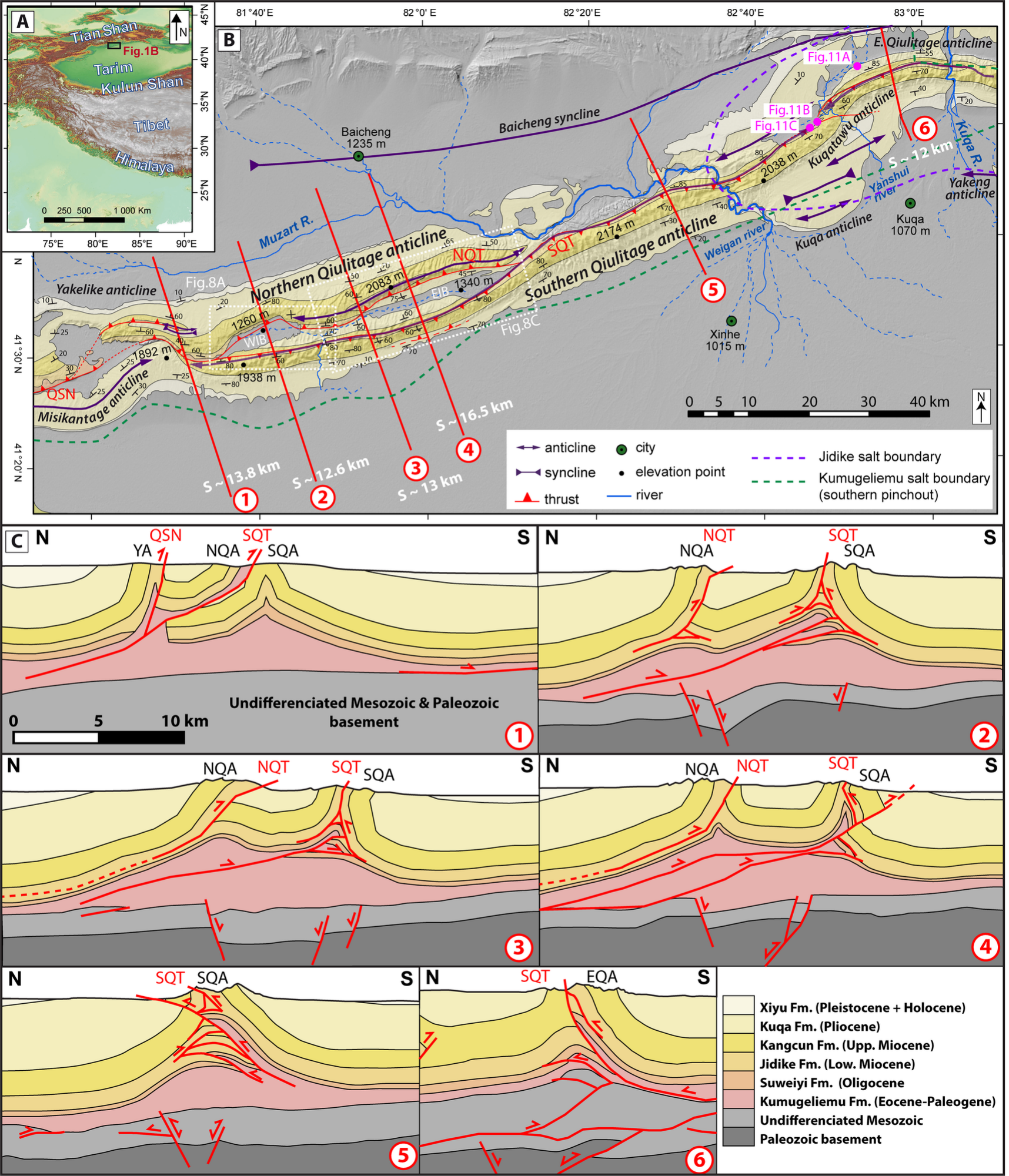
A
Tian Shan
Fig.1B
Tarim
Kulun Shan
Tibet
Himalaya
0 250 500 1 000 Km
75°E 80°E 85°E 90°E
45°N 40°N 35°N 30°N 25°N
B
81°40'E 82°0'E 82°20'E 82°40'E 83°0'E
41°30'N 41°20'N
Baicheng
1235 m
Baicheng syncline
E. Qiulitage anticline
Fig.11A
Fig.11B
Fig.11C
Kuqatawu anticline
2038 m
Kuqa R.
S ~ 12 km
Yanshui river
Yakeng anticline
Kuqa
1070 m
Muzart R.
Northern Qiulitage anticline
NQT
SQT
2174 m
Southern Qiulitage anticline
Weigan river
Kuqa anticline
Yakelike anticline
Fig.8A
2083 m
1340 m
EJB
1260 m
WJB
892 m
1938 m
Fig.8C
Xinhe
1015 m
QSN
Misikantage anticline
S ~ 16.5 km
S ~ 13.8 km
S ~ 12.6 km
S ~ 13 km
0 5 10 20 30 40 km
anticline
syncline
thrust
city
elevation point
river
Jidike salt boundary
Kumugeliemu salt boundary (southern pinchout)
C
N S
QSN SQT
YA NQA SQA
NQT
Undifferenciated Mesozoic & Paleozoic basement
0 5 10 km
SQT EQA
Xiyu Fm. (Pleistocene + Holocene)
Kuqa Fm. (Pliocene)
Kangcun Fm. (Upp. Miocene)
Jidike Fm. (Low. Miocene)
Suweiyi Fm. (Oligocene
Kumugeliemu Fm. (Eocene-Paleogene)
Undifferenciated Mesozoic
Paleozoic basement

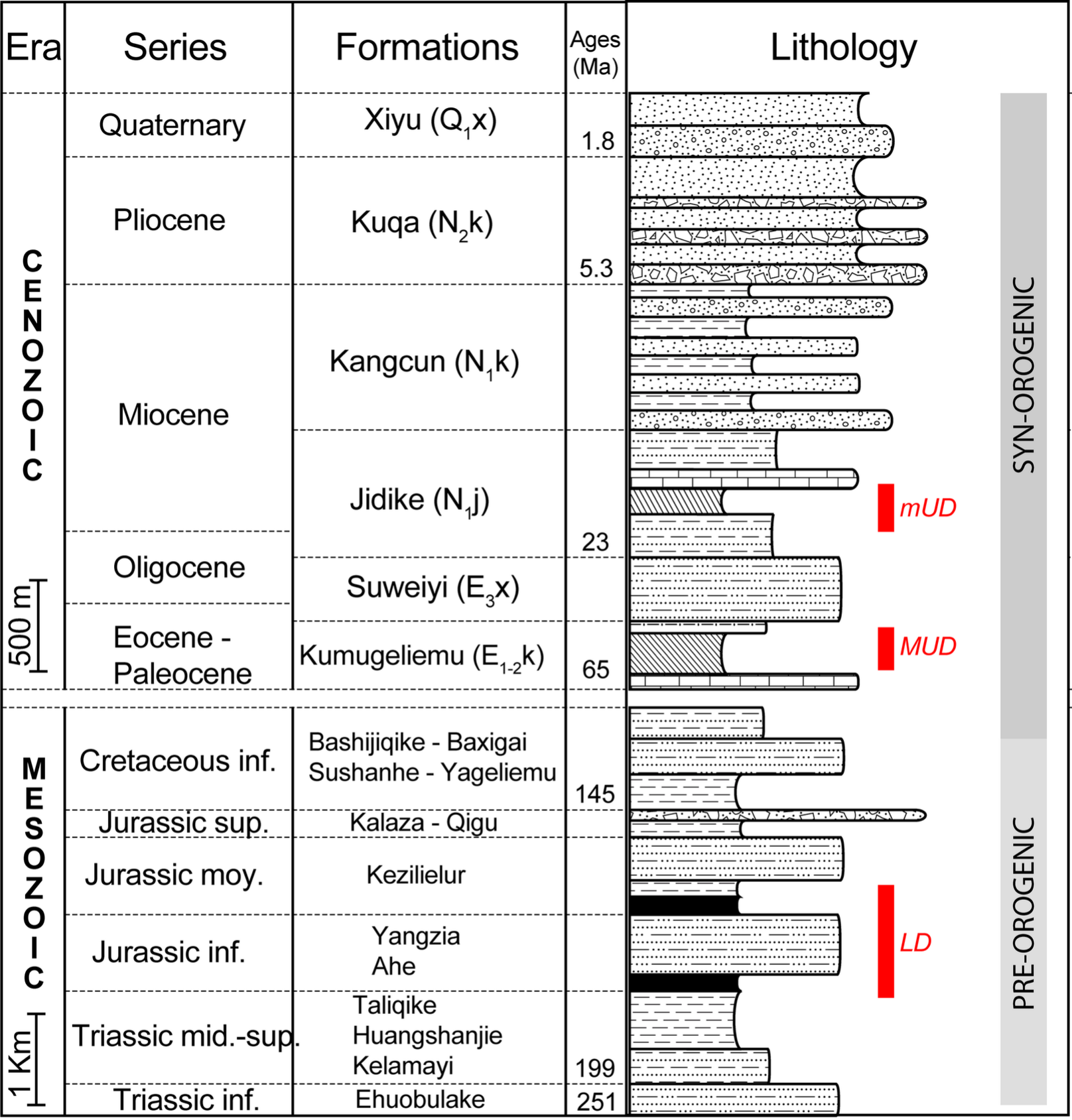
Era
Series
Formations
Ages (Ma)
Lithology
CENOZOIC
MESOZOIC
Quaternary
Xiyu (Q_1x)
1.8
Pliocene
Kuqa (N_2k)
5.3
Miocene
Kangcun (N_1k)
Jidike (N_1j)
23
Oligocene
Suweiyi (E_3x)
Eocene - Paleocene
Kumugeliemu ($E_{1-2}k$)
65
Cretaceous inf.
Bashijiqike - Baxigai
Sushanhe - Yageliemu
145
Jurassic sup.
Kalaza - Qigu
Jurassic moy.
Kezilielur
Jurassic inf.
Yangzia
Ahe
Triassic mid.-sup.
Taliqike
Huangshanjie
Kelamayi
199
Triassic inf.
Ehuobulake
251
500 m
1 Km
mUD
MUD
LD
SYN-OROGENIC
PRE-OROGENIC
conglomerate
pebble
sandstone
limestone
alternating siltstone / rough sandstone
alternating siltstone / sandstone
siltstone
coal
evaporite

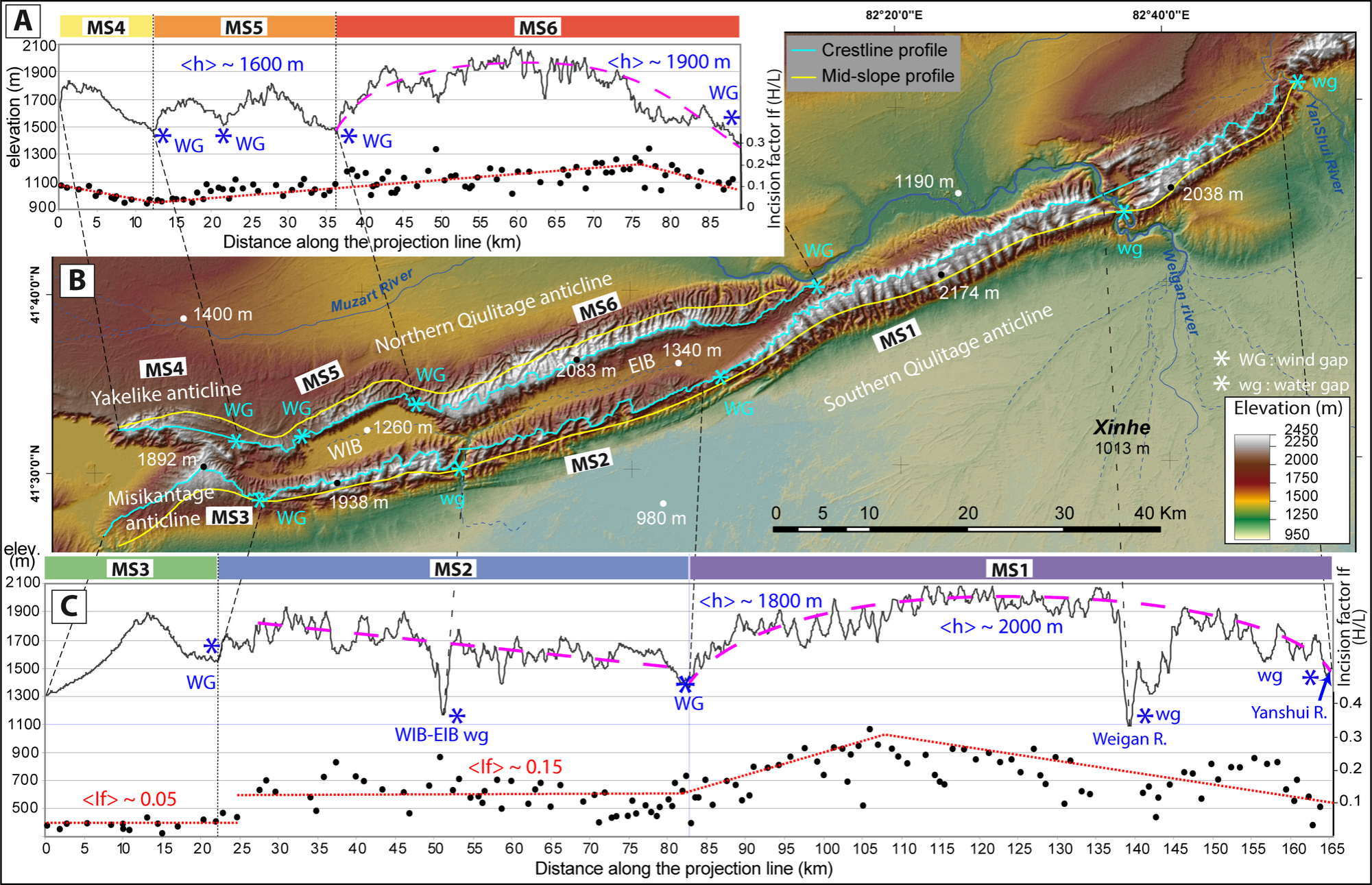
A
MS4
MS5
MS6
<h> ~ 1600 m
<h> ~ 1900 m
WG
elevation (m)
Incision factor If (H/L)
Distance along the projection line (km)
Crestline profile
Mid-slope profile
82°20'0"E
82°40'0"E
41°40'0"N
41°30'0"N
B
1400 m
Muzart River
Northern Qiulitage anticline
MS6
MS4
Yakelike anticline
MS5
WG
2083 m
EIB
1340 m
1260 m
WIB
1892 m
Misikantage anticline
MS3
1938 m
wg
MS2
980 m
MS1
Southern Qiulitage anticline
1190 m
2038 m
2174 m
Yanshui River
Weigan river
Xinhe
1013 m
WG : wind gap
wg : water gap
Elevation (m)
2450
2250
2000
1750
1500
1250
950
0 5 10 20 30 40 Km
elev. (m)
C
<h> ~ 1800 m
<h> ~ 2000 m
WIB-EIB wg
Weigan R.
Yanshui R.
<If> ~ 0.05
<If> ~ 0.15
Incision factor If (H/L)

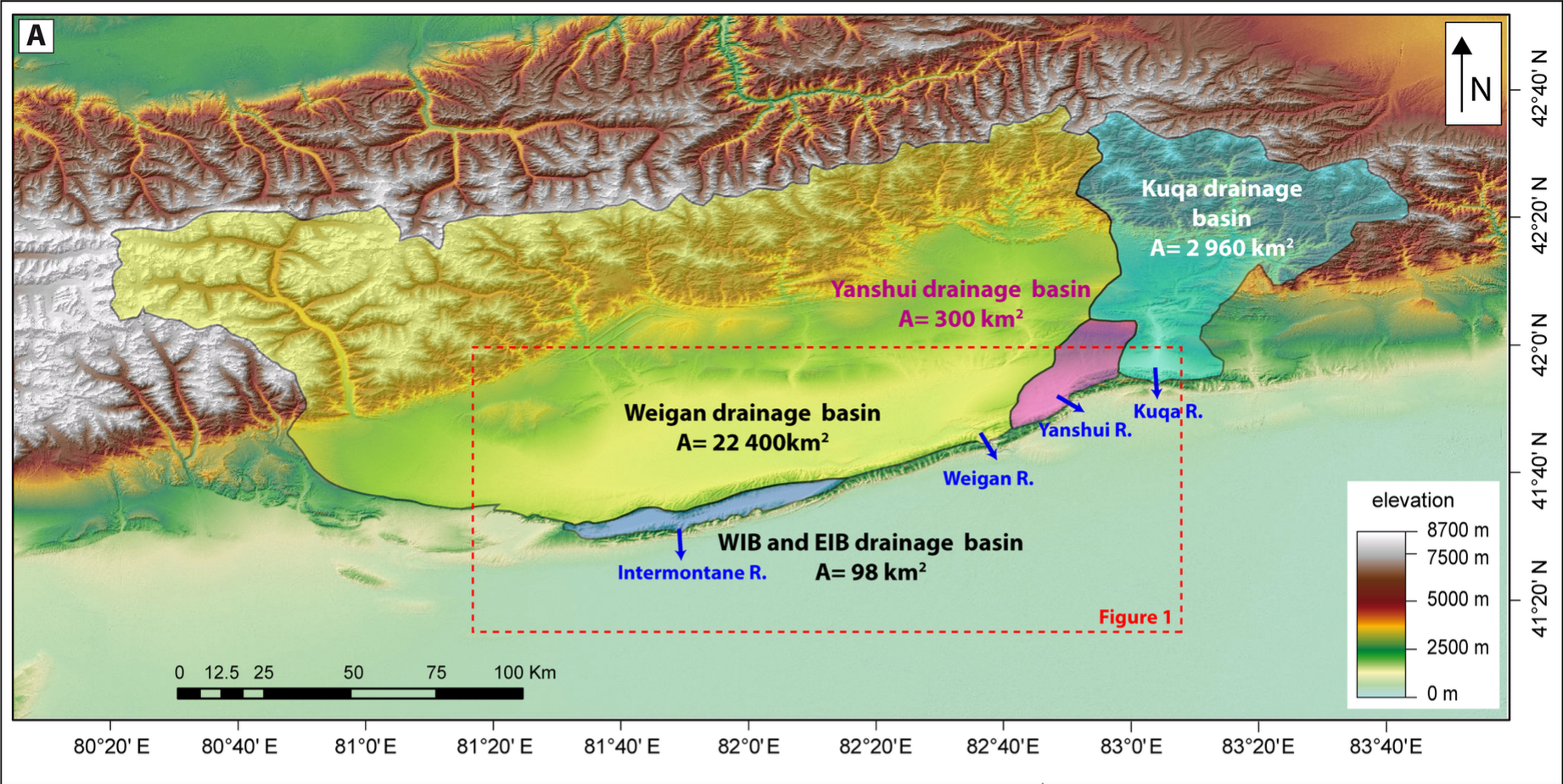
A
N
Kuqa drainage basin
A= 2 960 km²
Yanshui drainage basin
A= 300 km²
Weigan drainage basin
A= 22 400km²
Kuqa R.
Yanshui R.
Weigan R.
WIB and EIB drainage basin
A= 98 km²
Intermontane R.
Figure 1
elevation
8700 m
7500 m
5000 m
2500 m
0 m
0 12.5 25 50 75 100 Km
42°40' N
42°20' N
42°0' N
41°40' N
41°20' N
80°20' E
80°40' E
81°0' E
81°20' E
81°40' E
82°0' E
82°20' E
82°40' E
83°0' E
83°20' E
83°40' E

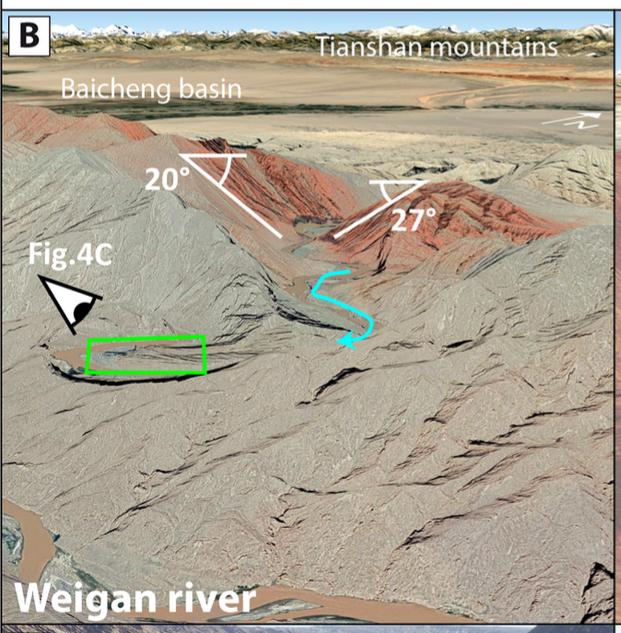
B
Tianshan mountains
Baicheng basin
20°
27°
Fig.4C
Weigan river

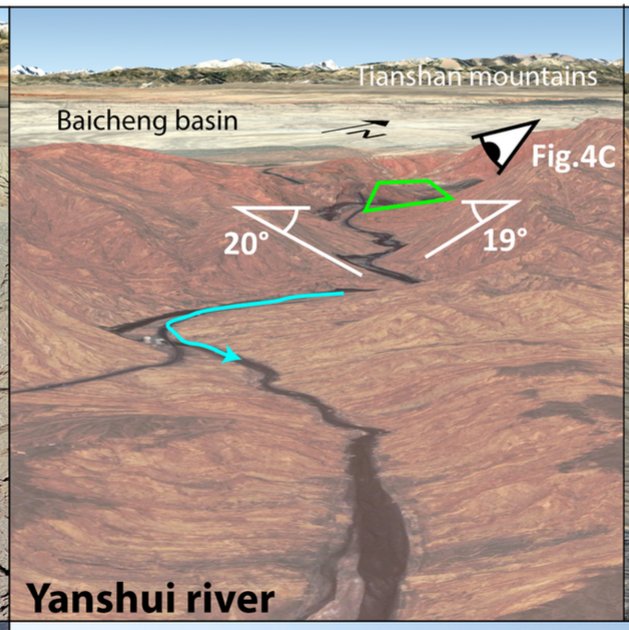
Tianshan mountains
Baicheng basin
Fig.4C
20°
19°
Yanshui river

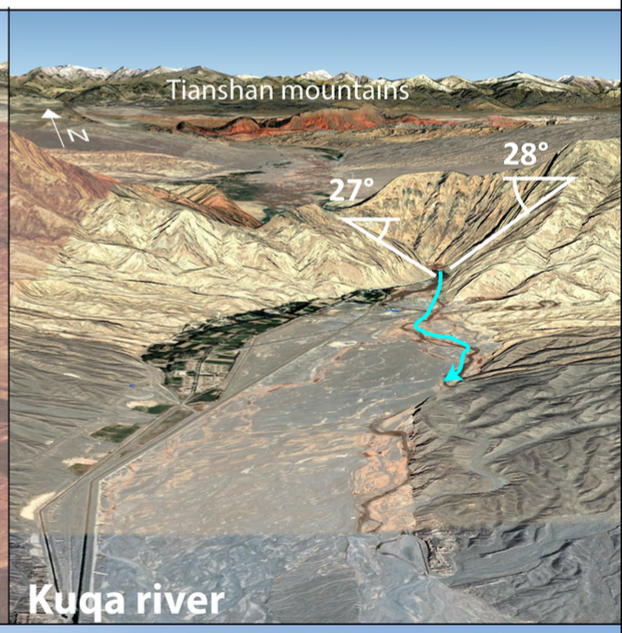
Tianshan mountains
N
28°
27°
Kuqa river

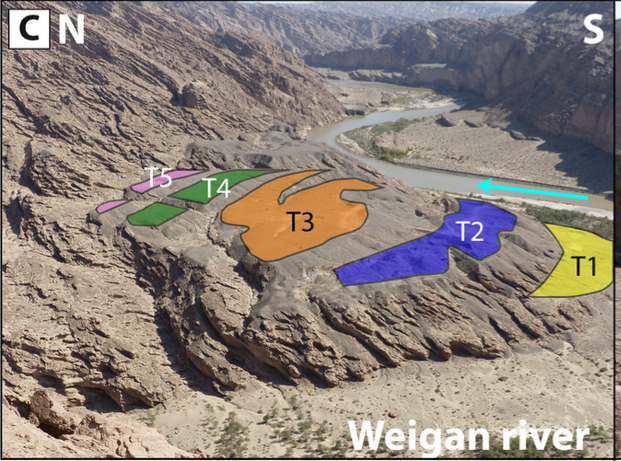
C
N
S
T5
T4
T3
T2
T1
Weigan river


SE
NW
T3
T2
T1
Yanshui river

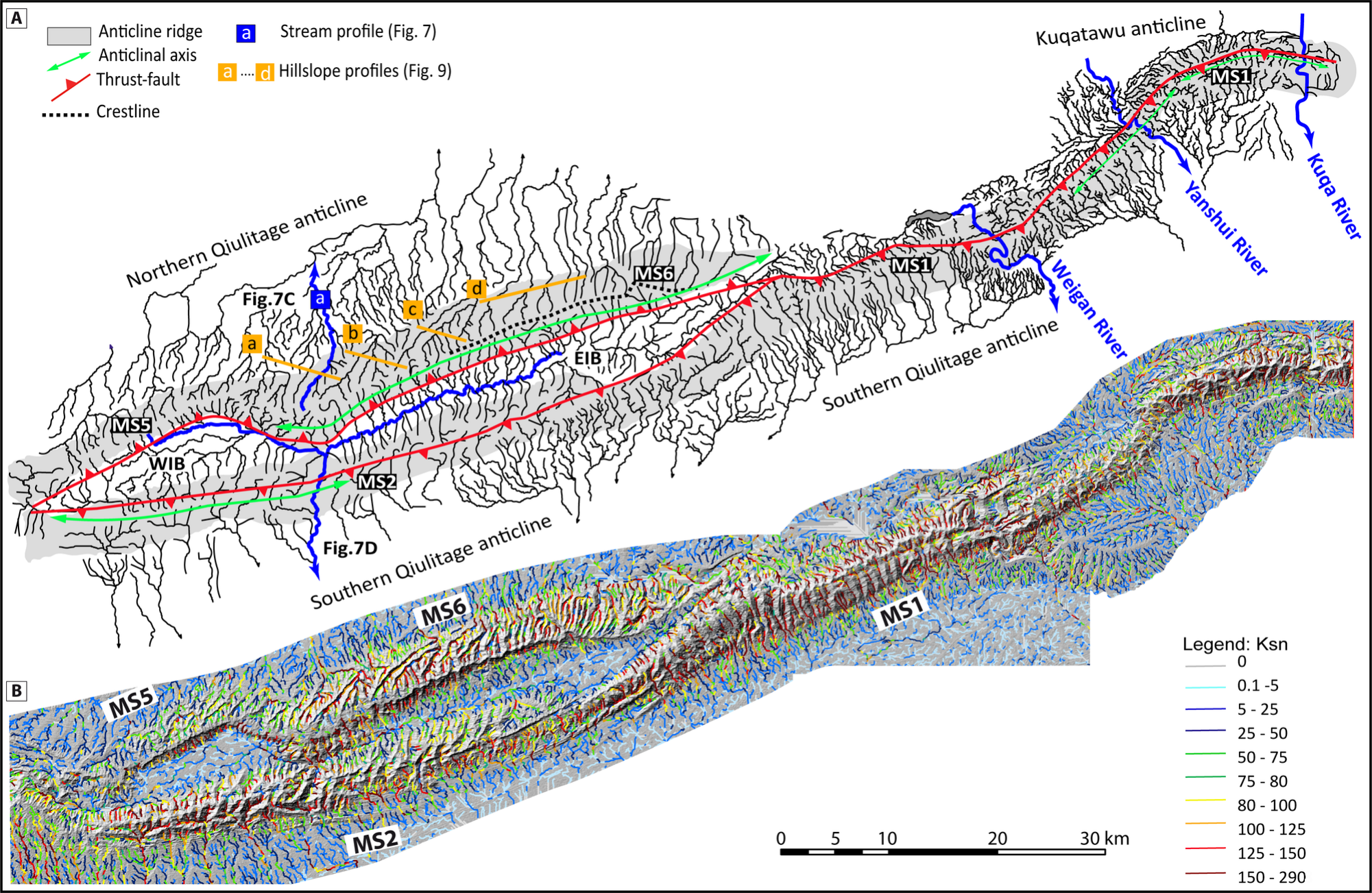
A
Anticline ridge
Anticlinal axis
Thrust-fault
Crestline
a Stream profile (Fig. 7)
a .... d Hillslope profiles (Fig. 9)
Kuqatawu anticline
MS1
Kuqa River
Yanshui River
Weigan River
Northern Qiulitage anticline
Fig.7C
a
b
c
d
MS6
MS1
EIB
Southern Qiulitage anticline
MS5
WIB
MS2
Fig.7D
Southern Qiulitage anticline
MS6
MS1
B
MS5
MS2
0 5 10 20 30 km
Legend: Ksn
0
0.1 -5
5 - 25
25 - 50
50 - 75
75 - 80
80 - 100
100 - 125
125 - 150
150 - 290

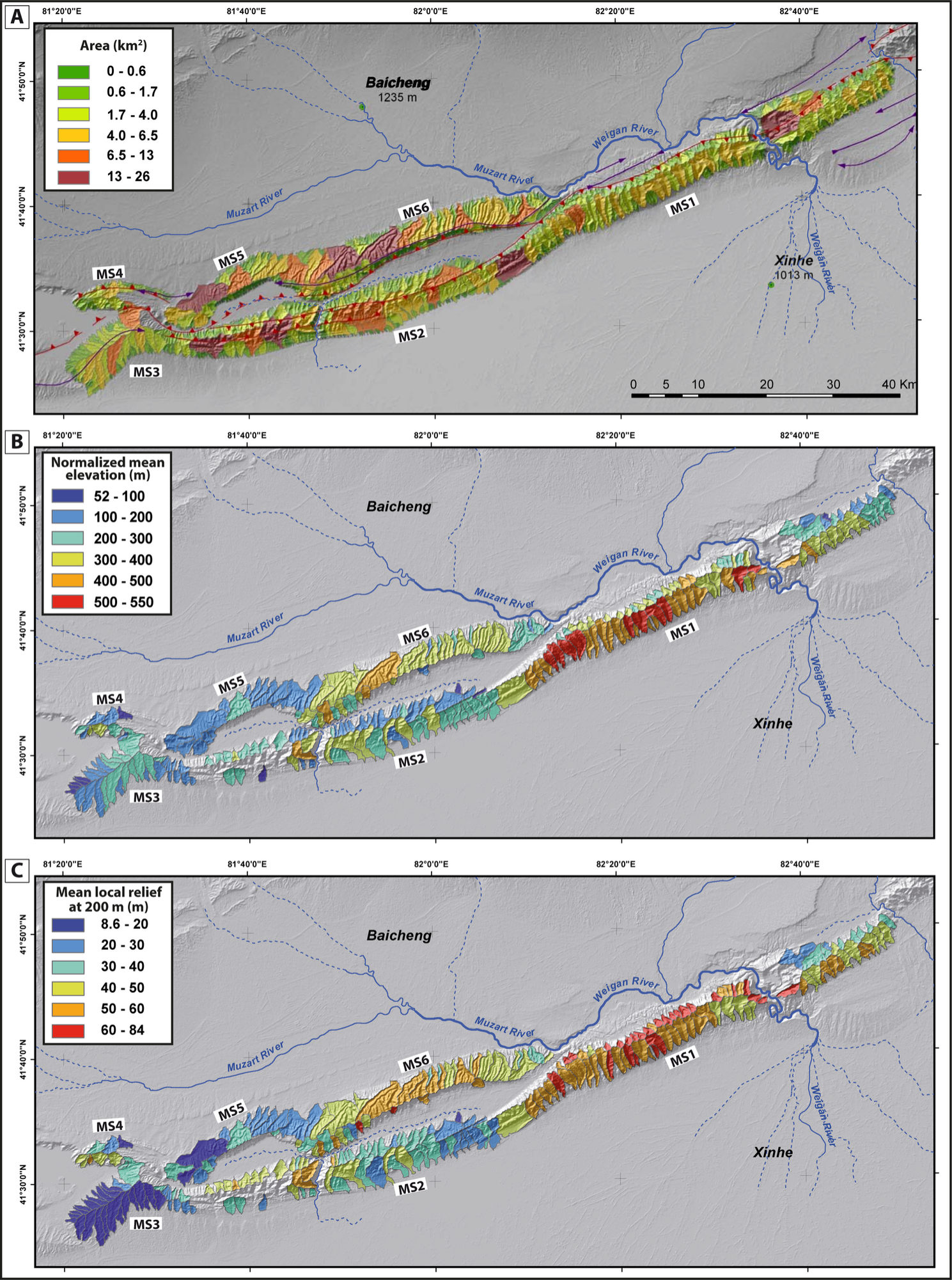
A
Area (km²)
0 - 0.6
0.6 - 1.7
1.7 - 4.0
4.0 - 6.5
6.5 - 13
13 - 26
Baicheng
1235 m
Xinhe
1013 m
Muzart River
Weigan River
MS1
MS2
MS3
MS4
MS5
MS6
0 5 10 20 30 40 Km
B
Normalized mean elevation (m)
52 - 100
100 - 200
200 - 300
300 - 400
400 - 500
500 - 550
C
Mean local relief at 200 m (m)
8.6 - 20
20 - 30
30 - 40
40 - 50
50 - 60
60 - 84
81°20'0"E
81°40'0"E
82°0'0"E
82°20'0"E
82°40'0"E
41°50'0"N
41°40'0"N
41°30'0"N

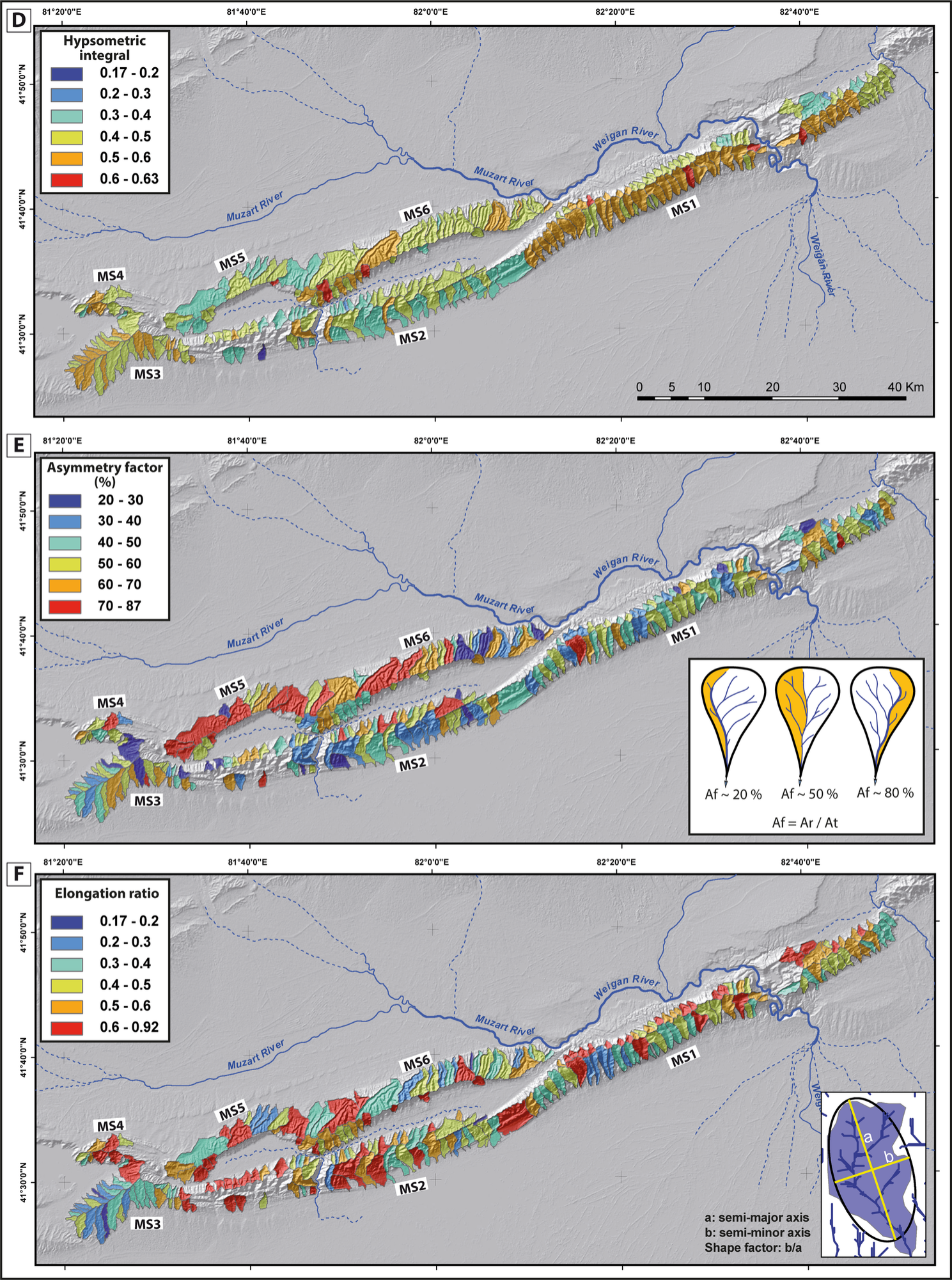
D
Hypsometric integral
0.17 - 0.2
0.2 - 0.3
0.3 - 0.4
0.4 - 0.5
0.5 - 0.6
0.6 - 0.63
81°20'0"E
81°40'0"E
82°0'0"E
82°20'0"E
82°40'0"E
41°50'0"N
41°40'0"N
41°30'0"N
Muzart River
Weigan River
MS1
MS2
MS3
MS4
MS5
MS6
0 5 10 20 30 40 Km
E
Asymmetry factor (%)
20 - 30
30 - 40
40 - 50
50 - 60
60 - 70
70 - 87
Af ~ 20 %
Af ~ 50 %
Af ~ 80 %
Af = Ar / At
F
Elongation ratio
0.17 - 0.2
0.2 - 0.3
0.3 - 0.4
0.4 - 0.5
0.5 - 0.6
0.6 - 0.92
a
b
a: semi-major axis
b: semi-minor axis
Shape factor: b/a

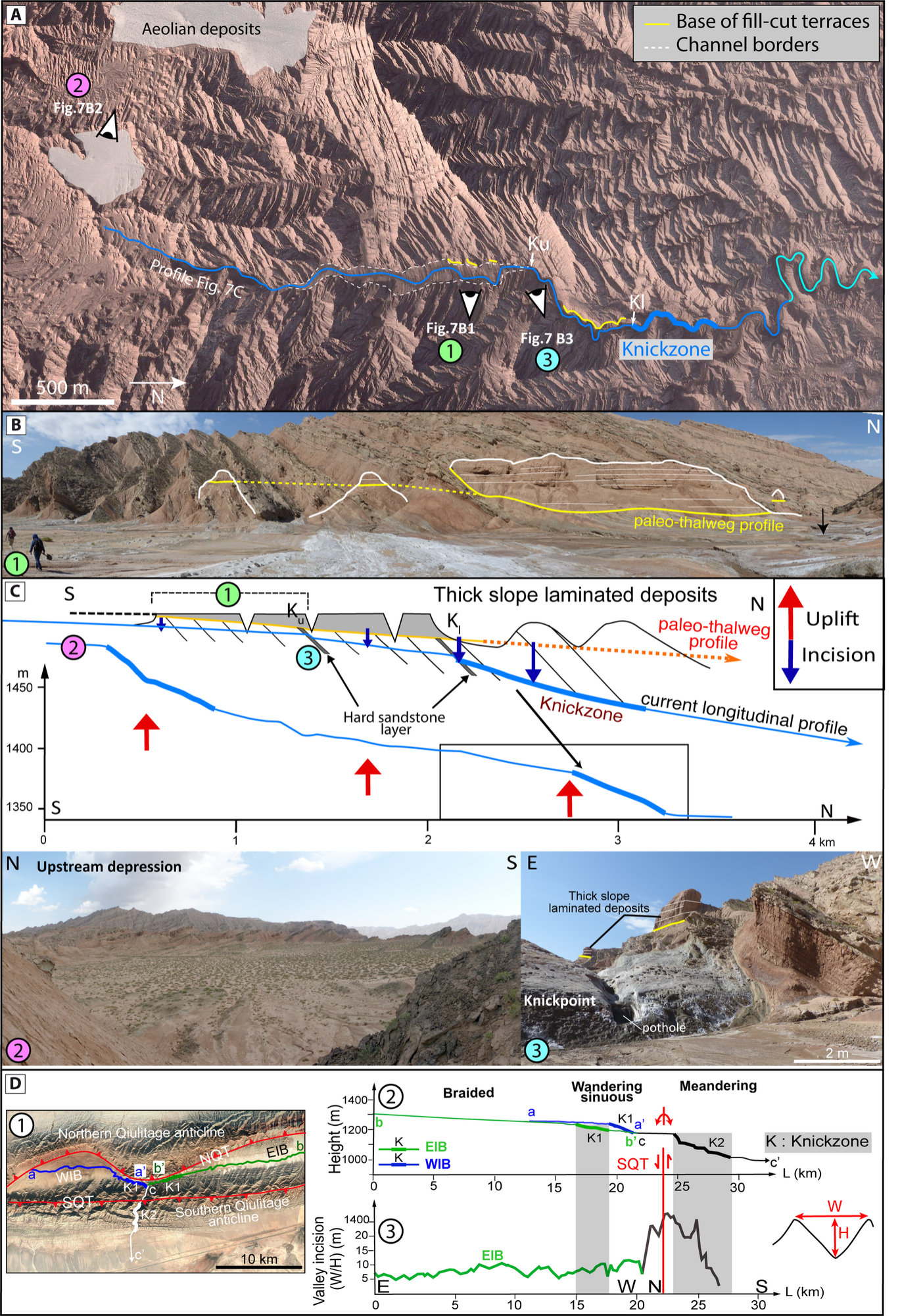
A
Aeolian deposits
Base of fill-cut terraces
Channel borders
2
Fig.7B2
Profile Fig. 7C
Ku
Kl
Fig.7B1
1
Fig.7 B3
3
Knickzone
500 m
N
B
S
N
paleo-thalweg profile
1
C
S
1
Ku
Kl
Thick slope laminated deposits
N
paleo-thalweg profile
Uplift
Incision
2
3
Hard sandstone layer
Knickzone
current longitudinal profile
m
1450
1400
1350
S
N
0
1
2
3
4 km
N
Upstream depression
S
E
W
Thick slope laminated deposits
Knickpoint
pothole
2 m
2
3
D
1
Northern Qiulitage anticline
NQT
EIB
b
a
WIB
a'
b'
K1
c
K1
SQT
K2
Southern Qiulitage anticline
c'
10 km
2
Braided
Wandering sinuous
Meandering
Height (m)
1400
1200
1000
a
b
K1
a'
K1
b'
c
K2
K
EIB
K
WIB
SQT
c'
L (km)
0
5
10
15
20
25
30
K : Knickzone
3
Valley incision (W/H) (m)
1400
20
15
10
5
EIB
E
W
N
S
L (km)
W
H

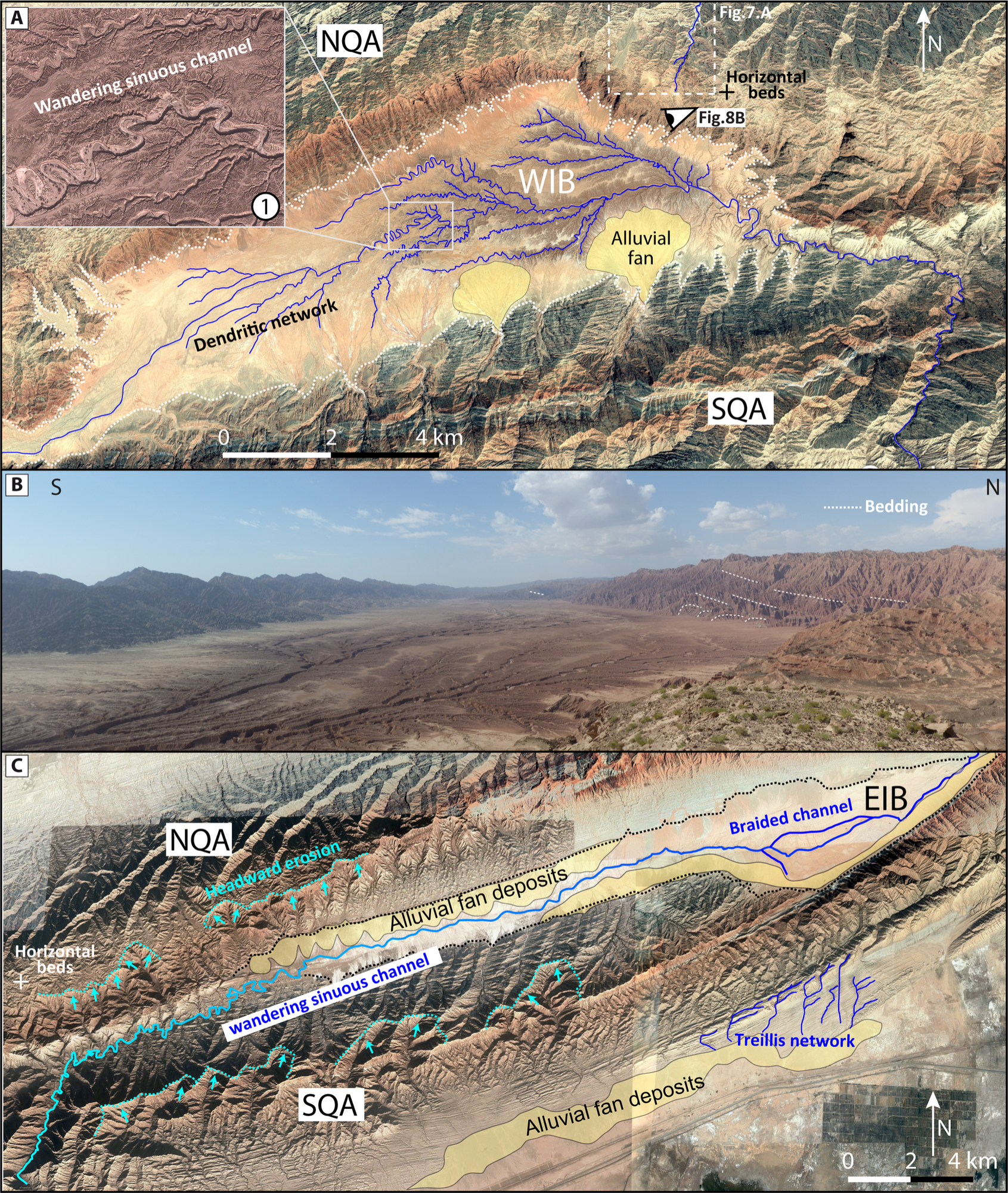
A
Wandering sinuous channel
1
NQA
Fig.7.A
N
Horizontal beds
Fig.8B
WIB
Alluvial fan
Dendritic network
SQA
0
2
4 km
B
S
N
Bedding
C
NQA
EIB
Braided channel
Headward erosion
Alluvial fan deposits
Horizontal beds
wandering sinuous channel
Treillis network
SQA
Alluvial fan deposits
N
0
2
4 km

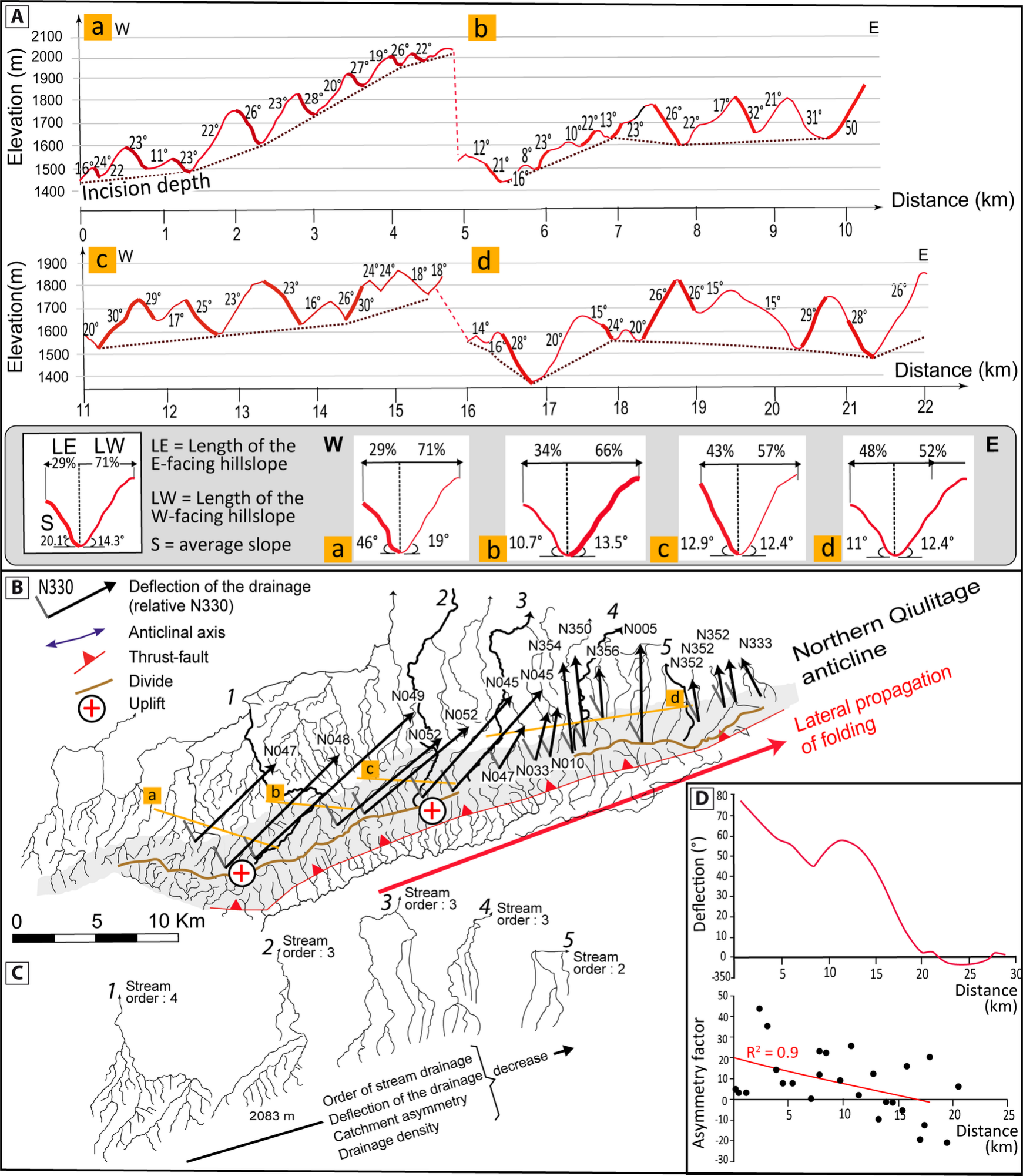
A
a W
b E
Elevation (m)
Incision depth
Distance (km)
c W
d E
Elevation(m)
Distance (km)
LE LW
29% 71%
S
20.1° 14.3°
LE = Length of the E-facing hillslope
LW = Length of the W-facing hillslope
S = average slope
W
E
29% 71%
46° 19°
34% 66%
10.7° 13.5°
43% 57%
12.9° 12.4°
48% 52%
11° 12.4°
B
N330
Deflection of the drainage (relative N330)
Anticlinal axis
Thrust-fault
Divide
Uplift
Northern Qiulitage anticline
Lateral propagation of folding
0 5 10 Km
C
Stream order : 4
Stream order : 3
Stream order : 3
Stream order : 3
Stream order : 2
2083 m
Order of stream drainage
Deflection of the drainage
Catchment asymmetry
Drainage density
decrease
D
Deflection (°)
Distance (km)
Asymmetry factor
R² = 0.9
Distance (km)

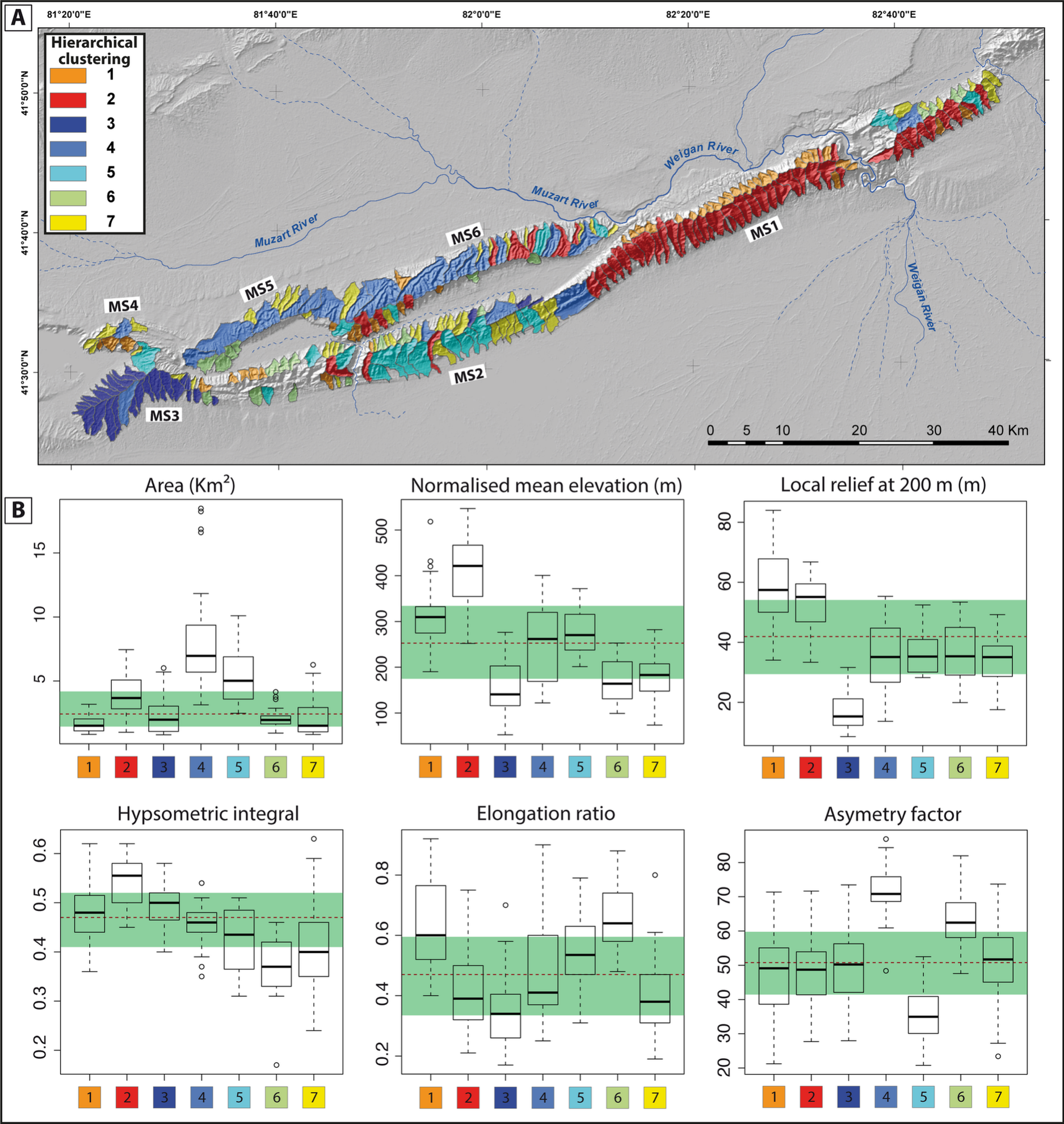
A
81°20'0"E
81°40'0"E
82°0'0"E
82°20'0"E
82°40'0"E
41°50'0"N
41°40'0"N
41°30'0"N
Hierarchical clustering
1
2
3
4
5
6
7
Muzart River
Muzart River
Weigan River
Weigan River
MS1
MS2
MS3
MS4
MS5
MS6
0 5 10 20 30 40 Km
B
Area (Km²)
Normalised mean elevation (m)
Local relief at 200 m (m)
Hypsometric integral
Elongation ratio
Asymetry factor

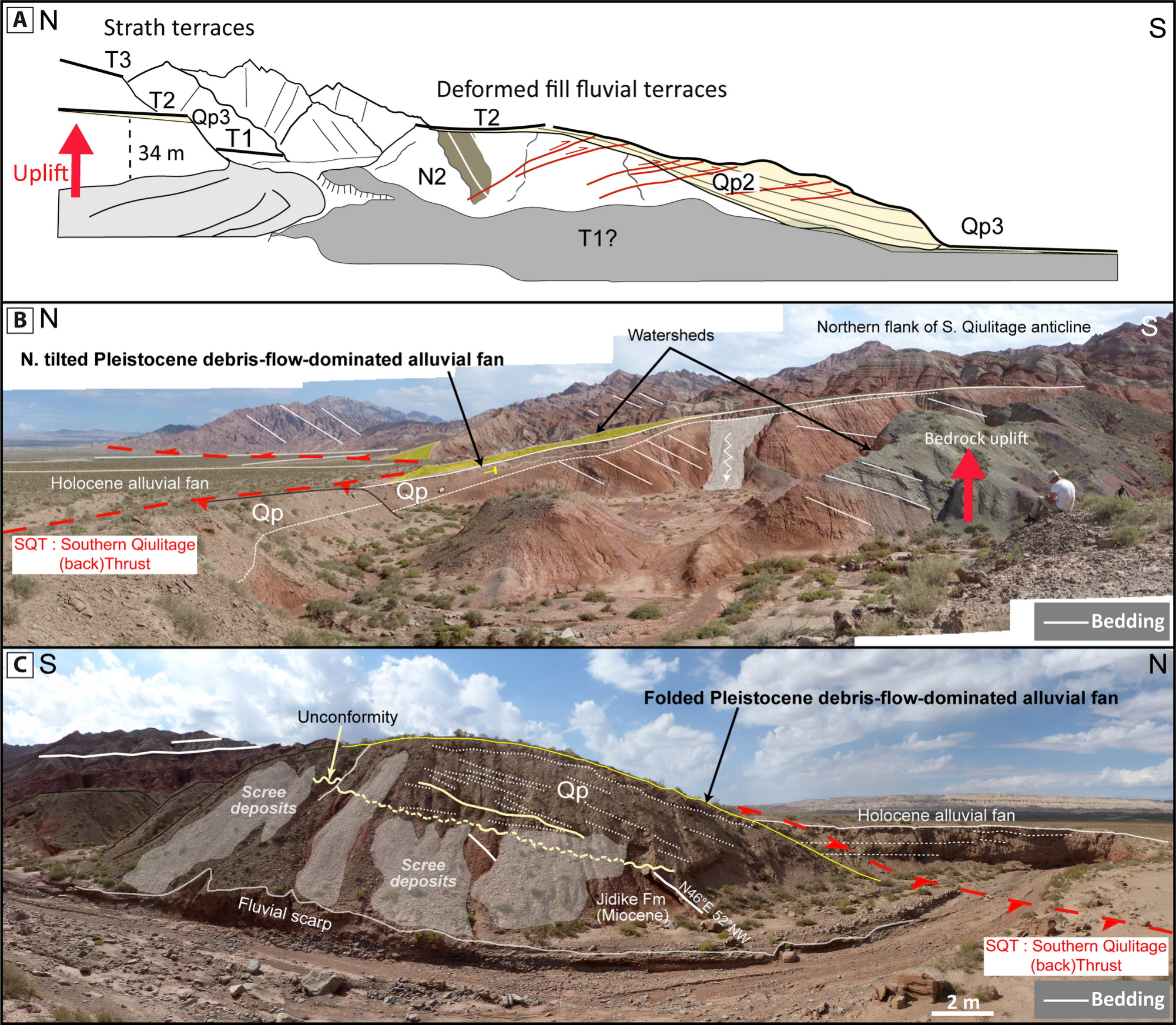
A
N
S
Strath terraces
T3
T2
Qp3
T1
34 m
Uplift
Deformed fill fluvial terraces
T2
N2
Qp2
Qp3
T1?
B
N
S
N. tilted Pleistocene debris-flow-dominated alluvial fan
Watersheds
Northern flank of S. Qiulitage anticline
Bedrock uplift
Holocene alluvial fan
Qp
Qp
SQT : Southern Qiulitage (back)Thrust
Bedding
C
S
N
Folded Pleistocene debris-flow-dominated alluvial fan
Unconformity
Scree deposits
Qp
Holocene alluvial fan
Scree deposits
Fluvial scarp
Jidike Fm (Miocene)
N46°E 52°NW
SQT : Southern Qiulitage (back)Thrust
Bedding
2 m

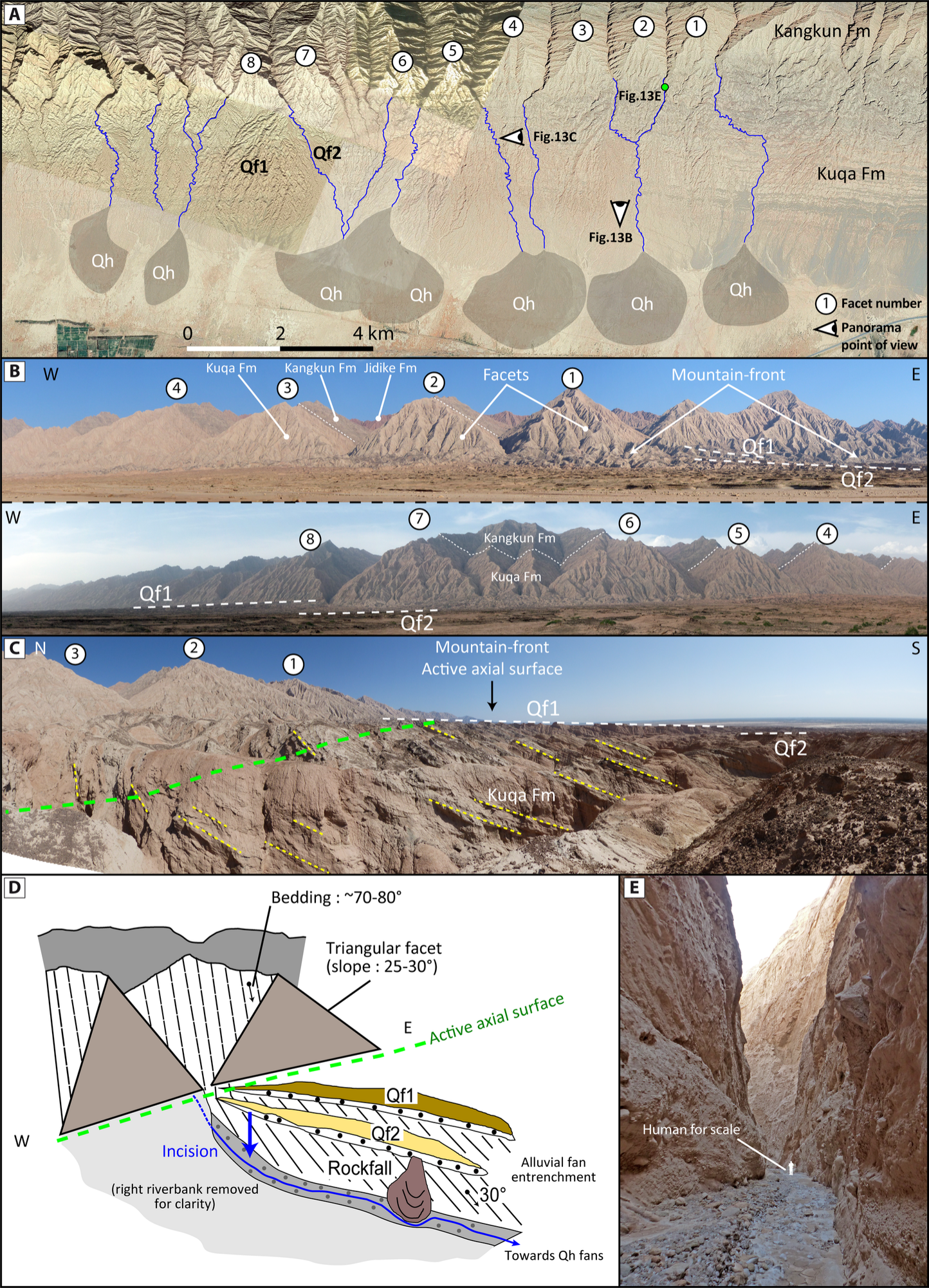
A
Kangkun Fm
Kuqa Fm
Fig.13E
Fig.13C
Fig.13B
Qf1
Qf2
Qh
0
2
4 km
Facet number
Panorama point of view
B
W
E
Kuqa Fm
Kangkun Fm
Jidike Fm
Facets
Mountain-front
Qf1
Qf2
C
N
S
Mountain-front
Active axial surface
Qf1
Qf2
Kuqa Fm
D
Bedding : ~70-80°
Triangular facet
(slope : 25-30°)
E
Active axial surface
W
Qf1
Qf2
Incision
Rockfall
30°
Alluvial fan
entrenchment
(right riverbank removed
for clarity)
Towards Qh fans
E
Human for scale

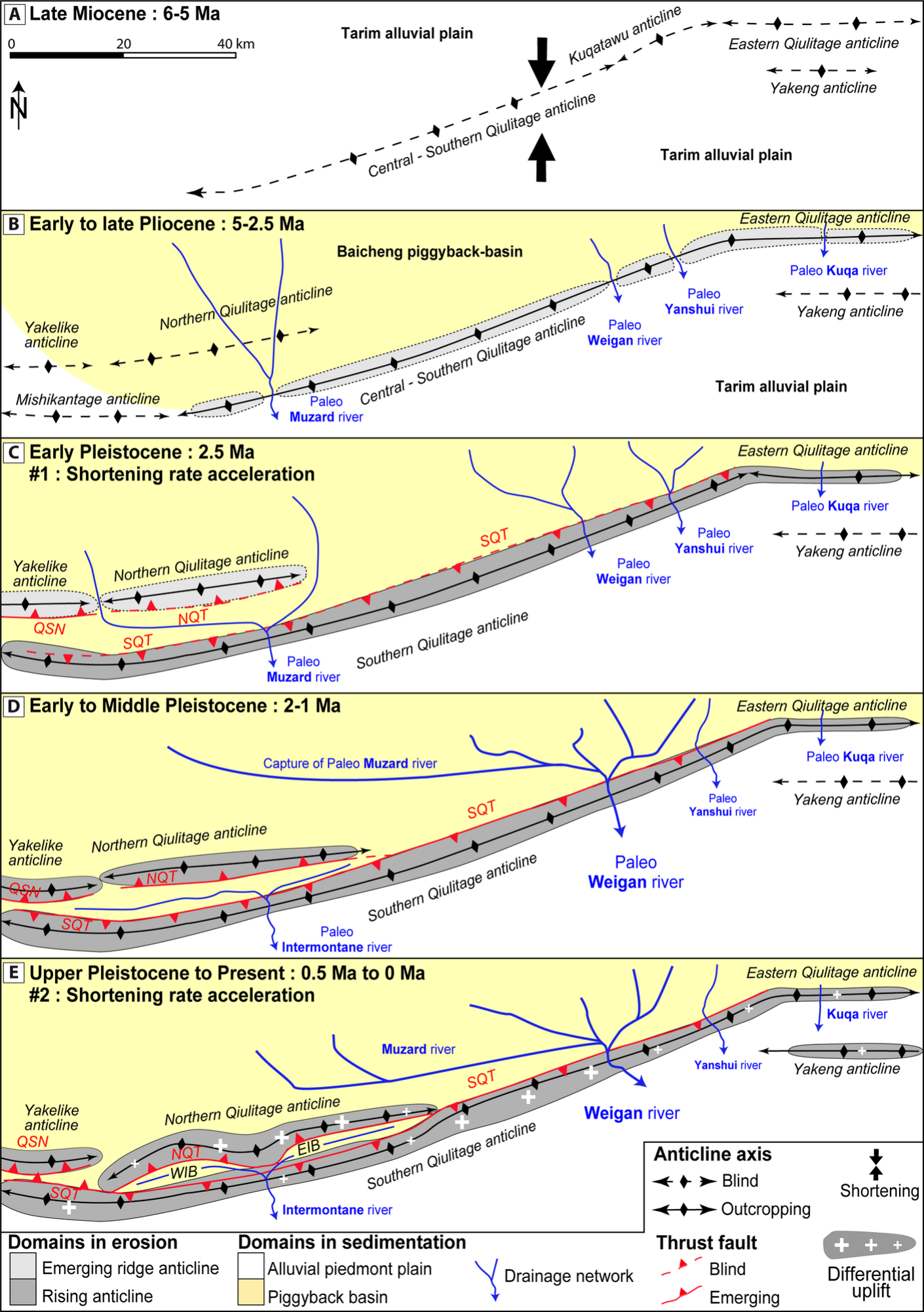
A Late Miocene : 6-5 Ma
0
20
40 km
N
Tarim alluvial plain
Kuqatawu anticline
Eastern Qiulitage anticline
Yakeng anticline
Central - Southern Qiulitage anticline
Tarim alluvial plain
B Early to late Pliocene : 5-2.5 Ma
Eastern Qiulitage anticline
Baicheng piggyback-basin
Paleo Kuqa river
Paleo Yanshui river
Yakeng anticline
Yakelike anticline
Northern Qiulitage anticline
Paleo Weigan river
Central - Southern Qiulitage anticline
Tarim alluvial plain
Mishikantage anticline
Paleo Muzard river
C Early Pleistocene : 2.5 Ma
#1 : Shortening rate acceleration
Eastern Qiulitage anticline
Paleo Kuqa river
SQT
Paleo Yanshui river
Yakeng anticline
Yakelike anticline
Northern Qiulitage anticline
Paleo Weigan river
QSN
NQT
SQT
Southern Qiulitage anticline
Paleo Muzard river
D Early to Middle Pleistocene : 2-1 Ma
Eastern Qiulitage anticline
Capture of Paleo Muzard river
Paleo Kuqa river
SQT
Paleo Yanshui river
Yakeng anticline
Yakelike anticline
Northern Qiulitage anticline
NQT
Paleo Weigan river
QSN
Southern Qiulitage anticline
SQT
Paleo Intermontane river
E Upper Pleistocene to Present : 0.5 Ma to 0 Ma
#2 : Shortening rate acceleration
Eastern Qiulitage anticline
Kuqa river
Muzard river
Yanshui river
Yakeng anticline
SQT
Yakelike anticline
Northern Qiulitage anticline
Weigan river
QSN
NQT
EIB
WIB
Southern Qiulitage anticline
SQT
Intermontane river
Anticline axis
Blind
Outcropping
Shortening
Domains in erosion
Emerging ridge anticline
Rising anticline
Domains in sedimentation
Alluvial piedmont plain
Piggyback basin
Drainage network
Thrust fault
Blind
Emerging
Differential uplift

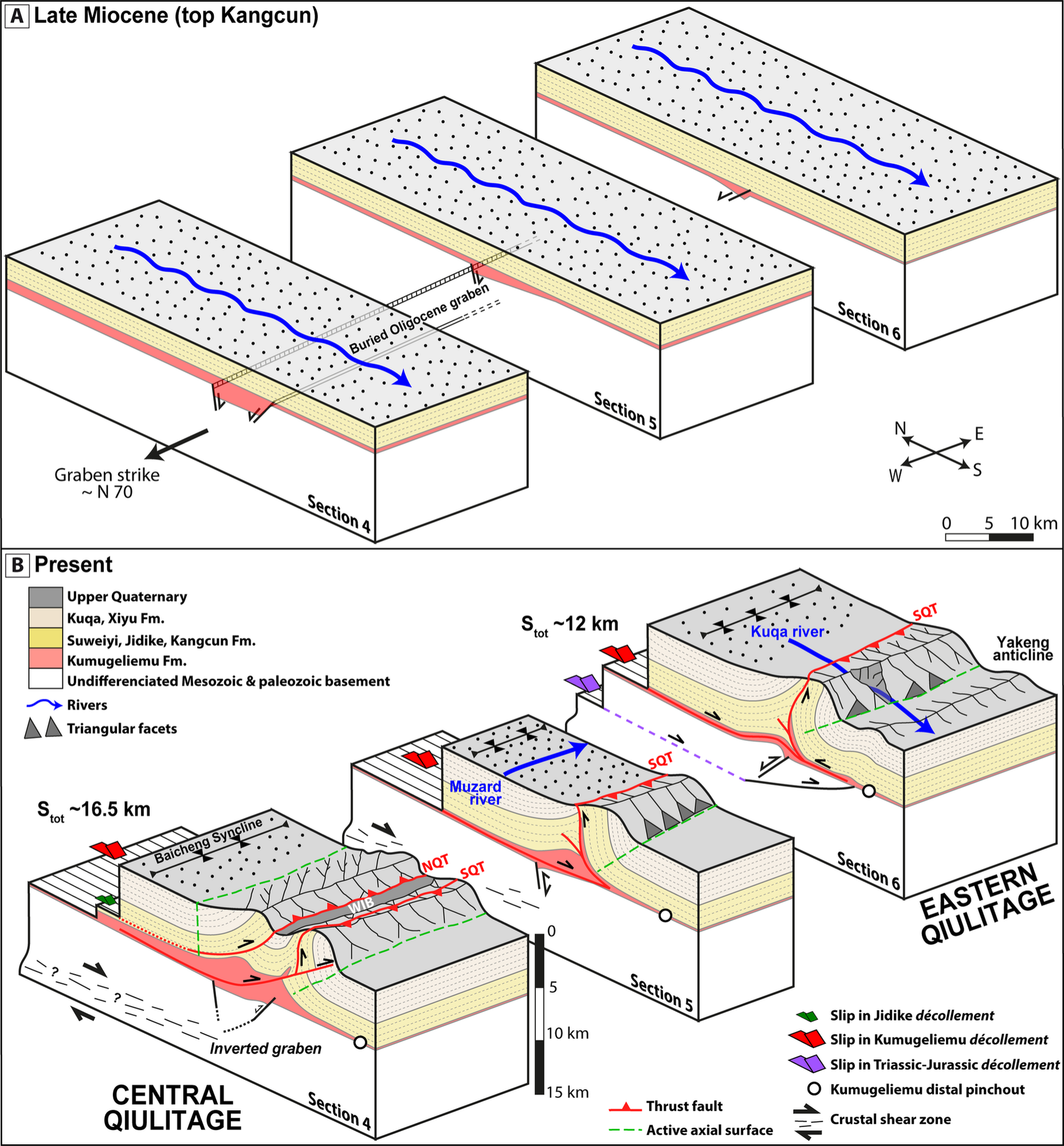
A Late Miocene (top Kangcun)
Buried Oligocene graben
Section 6
Section 5
Section 4
Graben strike
~ N 70
N
E
W
S
0 5 10 km
B Present
Upper Quaternary
Kuqa, Xiyu Fm.
Suweiyi, Jidike, Kangcun Fm.
Kumugeliemu Fm.
Undifferenciated Mesozoic & paleozoic basement
Rivers
Triangular facets
S tot ~12 km
Kuqa river
SQT
Yakeng anticline
Muzard river
S tot ~16.5 km
Baicheng Syncline
NQT
WIB
Inverted graben
EASTERN QIULITAGE
CENTRAL QIULITAGE
0
5
10 km
15 km
Slip in Jidike décollement
Slip in Kumugeliemu décollement
Slip in Triassic-Jurassic décollement
Kumugeliemu distal pinchout
Crustal shear zone
Thrust fault
Active axial surface

Variables	*Symbols*	*Interpretations*
Drainage basin		
Basin area	A	Geological structure, mean slope, age
Local relief	Δr (1)	Provides measure of the roughness of the topography and is controlled by climate and uplift rate at long sclaes
Hypsometric curve and integral	HI (2)	Form and evolution of drainage basin; Young, mature, old-age drainage pattern ; Growth of structures
Main slope	α (3)	
Basin asymmetry factor	A*f* (4)	It is calculated from the ratio between the right river bank width (Lr) and the total valley width (Ll)
Basin elongation ratio	Re (5)	Basin shape become more circular with time after cessation of ridge uplfit
Drainage pattern morphometry		
Fluvial incision factor	I*f* (6)	Differential erosion
Steepnes index	S (7)	where (k_s) and (θ) correspond to the steepness index and concavity index, respectively (e.g. Hack, 1957) Snyder et al., 2000), interpreted as as a transient profiles caused by an increase of uplift rate

(1) Δr : $\Delta z(l) = z(x+l)-z(x)$ where Δz is the local relief, z is the elevation, and l is the length scale

(2) HI: The hypsometric curve is defined to divide the heights and areas by the total heights and total area, respectively. Hypsometric analysis has been performed to summarize the form and evolution of drainage basins (Strahler, 1952).

(3) Main slope (α): we measure the average of slope values for each basin.

(4) VA=100.[Lr /(Lr+Ll)]

(5) Re= B*w*/B*l* ; The basin elongation ratio is defined as the ratio of the maximuml width of the drainage (B*w*) to its maximum length (B*l*)(Schumm, 1956; Bull & McFadden, 1977)

(6)I*f* Fluvial Incision factor If =100.[W/H] where W is the right and left riverbanks width, respectively, and H is the height between crestline

(7) $S = ks.A^{-\theta}$ Ks Stream gradient index

	Average of each parameter							
	A Area (km^2)	Minimum elevation (m)	Mean elevation (m)	Maximum elevation (m)	HI (Hypsometric integral)	α Mean slope (°)	Maximum slope (°)	A_f (Asymetry factor)
Northern morphostructures								
MS5	2.15	1365	1558	1796	0.44	19	43	56
MS6								
Northern flank	4.96	1280	1521	1805	0.45	20	47	57
Southern flank	2.24	1298	1595	1889	0.49	21	51	50
Southern morphostructures								
MS3								
Northern flank	1.49	1293	1442	1593	0.49	10	23	45
Southern flank	1.92	1296	1418	1541	0.50	8.3	20	55
MS2								
Northern flank	1.61	1289	1423	1630	0.40	16	35	55
Southern flank	4.94	995	1267	1679	0.39	17	50	44
MS1								
Northern flank	1.81	1316	1565	1885	0.42	24	47	48
Southern flank	3.85	1213	1619	1978	0.53	25	49	51